

24 depths of 1560 and 3927 m. The northern coast of Puerto Rico and its large offshore area are
25 underlain by a mid-Eocene and younger forearc basin topped by a thick carbonate platform.
26 There are no drillholes offshore and tying seismic lines across the shoreline there is problematic.
27 We describe our virtual outcrop and constrain its age and stratigraphy using 7 ROV rock samples
28 and compare them to deep boreholes and outcrops on land. Our formation descriptions and ages
29 agree for the most part with those on land, but we identified a 100 m thick section, represented
30 on land by an unconformity. Our stratigraphic interpretation indicates lateral variations in
31 formation thicknesses and establishes a cross-section for additional sampling of the Eocene-
32 Pliocene geology. It also suggests that Mona Rift has formed since mid-Pliocene. The presence
33 or absence of Fe-Mn crust on rocks along the transect may be correlated with the smoothness of
34 the rock surface.

35

36 **INTRODUCTION**

37 Geological exploration of Mars relies on remotely operated vehicles equipped with robotic
38 instrumentation (e.g., Squyres et al., 2009) Similar technological advances are lagging in
39 underwater geological exploration. Geological studies in the deep ocean (below the depth range
40 of human diving, for the most part, $> \sim 90$ m below sea surface) have utilized shipboard and
41 autonomous underwater vehicles (AUVs), mounted acoustic imaging, dredge samples, coring,
42 and grab samples taken by submersibles and remotely operated vehicles (ROVs) (e.g., Heezen et
43 al., 1985; Jakuba et al., 2011). Apart from acoustic imaging, these methods typically provide
44 information at discrete points, which is laterally extrapolated to understand the geological
45 environment. Near-seafloor acoustic imaging can provide high-resolution areal mapping of the

46 bathymetry at a scale approaching photography (Marx et al., 2000), but only visual observations
47 can provide geological context to discrete point observations and acoustic maps.

48

49 Visual observations of seafloor traverses by submersibles and ROV have been typically reduced
50 to bathymetric profiles, sample images, and feature interpretations (e.g., Stakes et al., 2006;
51 Micallef et al., 2012). Recent improvements in multi-processor parallel computing allow the
52 construction of photogrammetry from a string of overlapping video frames and the creation of
53 virtual outcrops in the deep ocean. Using virtual outcrops (e.g., Pringle et al., 2006), we can
54 implement some concepts of field geology at great ocean depths (1000-6000 m). For example,
55 we can map hard and soft beds, measure their apparent angle and attitude, describe and trace
56 textures on maps, and calibrate the geology using samples from sites located with precision of
57 several centimeters. Similar to field geology on land, the utility of virtual outcrop analysis can be
58 best applied to environments with high-angle outcrops, lithified rocks, and escarpments, and is
59 less useful in environments of low slope angles and high accumulation rates.

60

61 Here we describe, using a virtual outcrop analysis, a 2367 m tall escarpment between water
62 depths of 3927 m to 1560 m, which is part of the west wall of Mona Rift (Figure 1A), a deep
63 (>5000 m) and narrow (~30 km) rift oriented perpendicular to the Puerto Rico subduction zone
64 NW of Puerto Rico (Figure 1B). We compare the mapped section to surface outcrops and drilled
65 sections on the north shore of Puerto Rico, extending the geology of the island by about 100 km
66 offshore to the northwest across Mona Rift. The offshore geological exposure of the carbonate
67 platform provides new insights to the development of the platform and the opening of Mona Rift.

68

69 **Geological background of Puerto Rico and Mona Rift**

70 The basement in Puerto Rico is part of the Cretaceous to Paleogene Antilles Island Arc, which
71 formed above the North American plate as it was being subducted to the SW under the
72 Caribbean plate (Jolly et al., 2008). The island arc includes Cuba, Jamaica, Hispaniola, Puerto
73 Rico, and the Virgin Islands. The arc became extinct in the Eocene when the Caribbean-North
74 America convergence direction changed from NE-SW to E-W leading to a highly oblique
75 subduction direction ever since (Pindell and Kennan, 2009). Exhumation and deformation of the
76 island arc took place between 52 and 29 Ma (Roman et al., 2021) depositing volcanoclastic,
77 clastic, and carbonate rocks over the arc basement (Larue, 1994) probably in a fluvial-deltaic
78 environment (van Gestel et al., 1998). A carbonate shelf has formed around the arc complex
79 since Middle or Late Oligocene time. The shelf north of the island was tilted by $\sim 4^\circ$ at about 3.3-
80 3.6 Ma (Moussa et al., 1987) with its northern edge now at a water depth of 4000 m and its
81 southern edge being elevated by several hundreds of meters and exposed on the island (van
82 Gestel et al., 1998, ten Brink, 2005; Figure 1B).

83

84 Mona Rift, a N-S oriented deep chasm cuts perpendicular to the tilt direction of the margin
85 resulting in successively deeper rift rims to the north (Figure 1B). The rift may have formed by
86 E-W extension with the main normal fault on its eastern side (Mondziel et al., 2010, ten Brink et
87 al., 2023). The west wall of the rift which is equally steep was either formed by secondary
88 antithetic faults (Mondziel et al., 2010) or by landslide scarps (ten Brink et al., 2004) or by a
89 combination of both. Mondziel et al. (2010) proposed two phases of extension, a slow phase
90 during the Middle Oligocene to Mid-Miocene (~ 30 -11 Ma) with a total extension of 1.7 km, and
91 a rapid phase between the Late Miocene and Recent time with a total extension of ≥ 4.4 km.

92

93 Detailed descriptions of the sedimentary section exposed on land in northern Puerto Rico were
94 provided by Hubbard (1923), Zapp et al. (1948), Meyerhoff (1975), Monroe (1980), Seiglie and
95 Moussa (1984), and Ward et al. (2002), based on outcrops and logs of two deep boreholes and
96 additional shallow boreholes. 4CPR borehole, located 8 km east of Arecibo (Figure 1B), was
97 drilled in 1960 to a depth of 1961 m, and spanned the entire post upper Eocene sedimentary
98 sequence (Briggs, 1961). Toa Baja borehole 49 km east of Arecibo was drilled in 1989 to a depth
99 of 2704 m of which only the upper 585 m were sedimentary rocks (Larue, 1991).

100

101 The mountainous core of Puerto Rico is made of predominantly Lower Cretaceous to Middle
102 Eocene volcanic and plutonic rocks (Monroe, 1980). Upper Eocene and Oligocene siliciclastic
103 sediments cover the irregular basement surrounding the mountainous core (Figure 1D; Ward et
104 al., 2002). Eocene rocks include volcanoclastic sandstone interspersed with mafic and
105 intermediate lavas, tuffs, marly pelagic limestone, chert, and epiclastic deposits (Smith et al.,
106 1991). The basal part of the Oligocene San Sebastian Formation in outcrops consists of
107 conglomerate and sandstone. It is overlain by sandstone and mudstone with lignite layers, and is
108 topped by carbonaceous mudstone, fine sandstones, and thin layers of packstone and wackestone
109 (Ward et al., 2002, and references therein).

110

111 The overlying Lares Limestone (Figure 1D) fills topographic depressions within the San
112 Sebastian Formation onshore (Monroe, 1980) and consists mainly of indurated calcarenite
113 stratified in 0.1-1-meter-thick beds. The limestone contains abundant calcareous algae and large
114 foraminifers (Monroe, 1980). It represents the start of autochthonous carbonate deposition in

115 shallow seas with diminished terrestrial input, which lasted throughout the rest of the Tertiary.
116 The Cibao Formation is a spatially variable formation (Ward et al., 2002). The formation's
117 typical lithology is fossiliferous calcareous claystone and clayey wackestone with thin units of
118 mudstone and sandstone. In the central part of the island, however, it mostly consists of
119 limestone similar to the underlying Lares Formation, and in the western part of the island, the
120 typical lithology interfingers in the lower part with fan-delta deposits of volcanoclastic sandstone,
121 conglomerate and shale. (Ward et al., 2002). The Cibao Formation in 4CPR borehole is mostly
122 composed of calcarenite, with a few layers of calcareous claystone and dense limestone (Briggs,
123 1961).

124

125 The Aguada (Los Puertos) Formation (Figure 1D) consists of calcarenite grading upward into
126 massive limestone and dolomitic limestone (Ward et al., 2002 and references therein). Layers are
127 typically several meters thick. The Aguada Formation rests conformably on Cibao Formation
128 and has a sharp contact with the overlying Aymamón Limestone, distinguished by increasing bed
129 thickness, color, and possibly a karst surface (Monroe, 1980; Meyerhoff et al., 1983). The
130 Aymamón Limestone is a "thick-bedded to massive commonly quartz-free, very pure limestone"
131 (Monroe, 1980). The Quebradillas (Camuy) Limestone overlies a paleo-karst surface developed
132 on the Aymamón Limestone and comprises thin to medium bedded calcarenite, chalky
133 limestone, chalk, and sandstone (Monroe, 1980). Deposition of Quebradillas Limestone is
134 thought to be the uppermost widely deposited formation onshore and offshore northern Puerto
135 Rico. The deposition appears to have ended 3.3-3.6 Myr ago with the northward tilting of
136 northern Puerto Rico and its shelf (Moussa et al., 1987). The tilting was interpreted to be
137 geologically rapid (tens of thousands of years; ten Brink, 2005), because seismic reflectors are

138 parallel to each other up to the seafloor (Moussa et al., 1987, López-Venegas et al., 2008;
139 Mondziel et al., 2010) and do not show a fan pattern, as expected to form over a slowly tilting
140 substrate.
141
142 Seiglie and Moussa (1984) correlated the Middle or Late Oligocene to Pliocene sedimentation
143 with global sea level changes generating sequence stratigraphic cycles on a stable shelf. Ward et
144 al. (2002) mapped east-west and north-south variations in formation thickness and facies based
145 on outcrops and drill holes. Van Gestel et al. (1998) used seismic reflection data to extend the
146 interpretation of these formations offshore under the tilted carbonate platform east of Mona
147 Passage, suggesting the existence of Middle or Late Oligocene and Miocene depocenters close to
148 the northern edge of the titled shelf and thin depositional thickness along three axes, north of San
149 Juan, north of Arecibo and along the western end of the island.

150

151 **METHODOLOGY**

152 Seafloor imagery and sediment core samples were collected at water depths between 2870 and
153 1560 m by the ROV *Hercules* during Dive H1300 of the Ocean Exploration Trust expedition
154 NA-035 aboard the ship E/V *Nautilus* in 2013 (ten Brink et al., 2014). The ROV *Hercules*,
155 tethered to the ship via a second ROV, *Argus*, was equipped with a high-definition video camera,
156 a manipulating arm for collecting rock and biological samples, push cores for collecting
157 sediment samples, and equipment for sampling environmental water conditions (Figure 1C).
158 *Argus* hovered over *Hercules* throughout the dives providing additional illumination. Seafloor
159 imagery at water depths between 3927 and 3167 m was collected by the ROV *Deep Discoverer*
160 during Dive 04 of the NOAA's Ocean Exploration Program expedition EX1502 in 2015 aboard

161 the NOAA Ship *Okeanos Explorer* (Kennedy et al., 2015). The ROV *Deep Discoverer* tethered
162 to the *Okeanos Explorer*, via a second ROV, *Seirios*, was equipped with a high-definition video
163 camera. *Seirios* hovered over *Deep Discoverer* throughout the dives providing additional
164 illumination. The ROV *Deep Discoverer* did not collect samples.

165

166 The deep-water environment and the single ROV path pose limitations on the extraction of
167 photogrammetry from ROV videos. These limitations include artificial lighting source which is
168 distance-dependent and color-biased due to unequal spectral absorption by sea water (Lee et al.,
169 2015). Shadows on the images may be cast by the ROV because of the second hovering ROV
170 lights and the ROVs instrument may be captured in the video. The ROV executes a single
171 meandering path over the ground, not an overlapping grid of tracks. ROV navigation uses a
172 combination of a bottom-looking Doppler Velocity Log (DVL) and an ultra-short baseline
173 (USBL) acoustic transmitters and receivers between the vessel and a transponder on the ROV. A
174 CTD cast prior to the dive helped constrain the sound speed in water. USBL navigation for the
175 ROV had a positioning accuracy of 1°, (<2% of slant range; Bell et al., 2014) which is about 50
176 m in 2500 m of water. Furthermore, the navigation in the systems that we used was not
177 embedded in the collected images and the camera orientation and focal points were not fixed or
178 recorded. Additionally, the ROV may carry out different missions during a dive or focus on
179 specific elements by request of the mission scientists.

180

181 These operational limitations required an elaborate post-acquisition processing, described in
182 detail in Flores and ten Brink, *Photogrammetry of the deep seafloor from unmanned submersible*
183 *exploration*, in prep. A brief summary of the processing steps is described here:

- 184 1. Convert the videos to individual images.
- 185 2. Reduce the number of images by de-sampling them to one image per second.
- 186 3. Equalize the colors in each image and compensate for the differential absorption of light
187 components.
- 188 4. Mask unwanted areas of the images, such as the bottom of the ROV.
- 189 5. Build image groups and remove unnecessary images, such as images with poor lighting, and
190 images zooming on fauna or following fish.
- 191 6. Use photogrammetry software to identify points and to match these points between images
192 inside an image group.
- 193 7. Build a “camera path” based on these matched points between images, called “tie points” in
194 the software, resulting in a sparse tie-point cloud. This step in the process is called “alignment”
195 and is done either automatically or manually a few frames at a time depending on how much
196 surface texture and contrasts are inside the images. Unfortunately, navigation cannot be used to
197 guide the process of alignment, because of the navigation limitations in deep water.
- 198 8. Add navigation and pseudo-ground controls to georeference the photogrammetry. The pseudo-
199 ground control points are determined by averaging the ROV navigation during temporary ROV
200 rests on the bottom or during extended hovering close to the bottom in one spot.
- 201 9. Merge the small image groups into hour-long group sections.
- 202 10. Conduct final camera calibration to fit the merged image groups using the navigation with its
203 associated errors, deleting outliers in the process.
- 204 11. Develop dense clouds and 3D surfaces draping them with texture for geological
205 interpretation.

206

207 Most of the processing steps were carried out using Agisoft Metashape Pro©, except for step 3,
208 which also used OpenCV's Contrast Limited Adaptive Histogram Equalization (CLAHE)
209 algorithm in Python. 3-D manipulation and display of the virtual outcrops were carried out using
210 VOG Lime©. Prior to describing the virtual outcrop, we evaluated possible artifacts generated by
211 the photogrammetry process and discarded or ignored distorted parts of the images. The units
212 comprising the virtual outcrop were described by relatively uniform appearance of visual
213 characteristics such as talus, massive rocks, and layered rocks (Figure 3) and by uniform slope
214 angle. These units can span thicknesses between several tens of centimeters and a few tens of
215 meters. Other characteristics such as ledges, channels, and notches, the presence of patina,
216 dislodged rocks, and sediment flows were also noted. The slope of each visual rock unit was
217 measured. Where visually possible, we measured the apparent layer dip.

218

219 The *Hercules* ROV collected rock samples with its mechanical arm in seven locations as it was
220 moving from the deepest part of the transect upward (Table 1, Figures 2 and 3). In four of the
221 locations (samples 029, 030, 033, and 035), the samples were grabbed from an in-situ position in
222 a rock face. Samples 029 and 031 were grabbed from a slope with densely strewn rocks and
223 sample 032 was grabbed a few 10s of cm below an outcrop. Thus, an uncertainty in the depth of
224 some of the samples should be considered. The samples were cut and described on board. All
225 seven samples are carbonate rocks (Table 1, Figure 2). Their geological age was interpreted
226 using observed calcareous nanofossils within the samples. Sample processing required using a
227 razor blade to shave off sediment for slide preparation. One slide per sample was prepared using
228 standard smear slide techniques. Upon evaluating the quality of the smear slides, however,
229 another set was prepared using a suspension preparation technique, which allowed for better

230 dissemination and distribution of both the sediment and calcareous nannofossil specimens. To
231 prepare slides using suspension, fresh material was shaved off a sample using a razor blade and
232 then mixed in with a small amount of distilled water, about 10 mL, to create a slurry. After
233 thoroughly stirring the slurry, a small amount was siphoned off with a pipette and transferred
234 onto a glass coverslip. The coverslips were dried in an oven at 93°C (200°F). Once dried, the
235 coverslips were adhered to glass slides using Norland Optical Adhesive #61 and cured under
236 ultraviolet light. Semi-quantitative data was collected for each sample following the technique of
237 Styzen (1997). The biozonations of Backman et al (2012), and Waterman et al. (2017) were
238 referenced to interpret geologic age; and mikrotax.org (Young et al., 2022) was referenced for
239 taxonomy.

240

241 Legacy seismic lines in the vicinity of the dive transects (Figure 1A) include single-channel
242 seismic (SCS) reflection line EW9605 P-47 with airgun volume of 1385 cu.in. and shot interval
243 of 14 to 16 s, multichannel seismic line (MCS) EW9501 1289 with airgun volume of 8400 cu.in.,
244 shot interval of 30 s and a 4-km-long 160-channel receiver cable, and USGS line P-31 collected
245 in 2006 with airgun volume of 35 cu.in., shot interval of 15 s and a 1.2-km-long 24-channel
246 receiver cable. Standard processing was applied to the data followed by Stolt post-stack time
247 migration with water velocity to attenuate sea floor diffractions.

248

249 **RESULTS**

250 **Visual geological analysis**

251 Figure 3 shows a summary of the geological characteristics and slope angle along the dive
252 transect. The bottom 550 m of the transect comprises talus, which is covered in a few places by

253 rockfall. *In-situ* rocks are exposed in this part of the escarpment only in two intervals (Figure 4.1,
254 4.2). More extensive rock exposure including a downslope channel cut into a hard surface is
255 found between depths of 2650 and 2735 m (Figure 4.1). Most of the rock exposure is covered by
256 dark patina inferred from the dive samples (Figure 2, Table 1) to be hydrogenetic
257 ferromanganese (Fe-Mn) crusts (e.g., Conrad et al., 2017) except in the vicinity of the downslope
258 channel. Talus extends farther down to a depth of 2850 m with a few large layered and
259 overturned blocks sticking out of it. *In situ* rocks are exposed at the bottom 20 m of the dive
260 section and are covered by patina (Figure 4.2).

261
262 The long talus slope changes abruptly at 2315 to cliffs of layered rocks, which are covered with
263 patina and are punctuated by several short intervals of steep talus with partially buried rockfalls
264 (Figure 4.3). Thin layers are dominant between 2260-2190 m (Figure 4.4) and a layered rock
265 slope, partially covered by sediment, is observed between depths of 2190–2150 m. A massive
266 and very steep rock face with some patina-covered thin layers extends between 2150-2120 m and
267 is cut by a downslope channel (Figure 4.5). Several small rockfall scars with fresh scarps are
268 observed in this section. A 2-m deep ditch with a subvertical rock wall crosses this slope at 2119
269 m and may represent a fault trace. The slope becomes sedimented above the ditch (Figure 4.5) up
270 to a depth of up to 2070 m. Farther up, the slope steepens again exposing layers of variable
271 thickness and some scars from rockfalls. A bench at a depth of 2018 m is overlain by 6 m thick
272 block of tilted layers (Figure 4.6). The steep slope resumes but the rock face becomes more
273 massive with a few outcrops devoid of patina and having grey bands (Figures 3B, 4.6). Another
274 talus slope between depths of 1955 and 1917 m is overlain by an even more massive rock face,
275 which is mostly patina free. This rock face is dissected by relatively few layers and ledges which

276 are about 1 m thick (Figure 4.7). The top of this section is dominated by a smooth patina-free
277 rock surface incorporating solidified mass-transport debris and is covered by a prominent ledge
278 at a depth of 1832 m (Figure 4.8). A massive, steep ($\leq 85^\circ$), and patina-free rock face rises
279 upward for about 60 m (Figure 4.9). This rock face is capped by a ~4 m thick deformed layer at a
280 depth of 1767 m, which is free of patina. The deformed layer is truncated by a thin sub-
281 horizontal rock layer, covered by patina, which is the base of a broad sedimented plane with a
282 very gentle slope (Figure 4.9). The slope changes abruptly at ~1711 m to a 35 m high steep
283 massive rock without patina before grading back to almost flat sediment-covered slope (Figure
284 4.10). The top part of the dive section is steeper, comprising of rocky benches that are partly
285 covered by sediments. The rocks are covered with patina (Figure 4.11, 4.12).

286

287 **Interpretation**

288 The presence of dated samples throughout the transect (Table 1) allows us to correlate the dive
289 observations with known geological formations described onshore in Puerto Rico (Ward et al.,
290 2002; van Gestel et al., 1998; Larue, 1991; Briggs, 1961). Although the section is on the western
291 side of the Mona Rift, it is closer to Puerto Rico than to Hispaniola, leading us to prefer the
292 Puerto Rican stratigraphy as a reference. The comparison relies on the assumption of spatial
293 continuity of the carbonate platform and the underlying volcanoclastic sediments onshore (Ward
294 et al., 2002) and offshore (Seiglie and Moussa, 1984; van Gestel et al., 1998). Nevertheless,
295 variations in thickness and lithologies are expected to exist between the onshore geology and the
296 dive transect similar to those observed within the onshore geology (Ward et al., 2002).

297

298 Our correlation specifically uses the two following methods: (a) we predict the approximate
299 depths of formation boundaries from the dated geological samples, and (b) we match the
300 lithological appearance and slope angles along the dive transect to the lithology described in
301 4CPR borehole (Briggs, 1961) and in outcrops (Ward et al., 2002). The combined criteria
302 support our interpretation of the formations and ages encountered in the dive transect.

303

304 Sample descriptions, their locations and depths, their ages based on the nannofossils found in
305 them, and their age confidence are listed in Table 1. Images of the outcrops from which the
306 samples were taken are shown in Figures 4.1, 4.4, 4.6, 4.9, and 4.11. The dated samples from the
307 dive transect (blue circles in Figure 5) can be fit by a depth-age polynomial curve with a
308 correlation coefficient $R^2 > 0.99$ (Figure 5). Three curves (blue dashes) were calculated to
309 accommodate the minimum, average, and maximum ages of the dated samples. Ward et al.,
310 (2002) provides a time scale to the mapped formations on land (Table 2). Ward's time scale
311 (vertical green dash lines) allows us to predict the approximate depths of formation boundaries
312 along our dive transect (Table 2) and to compare them to the observed lithological changes
313 within some acceptable uncertainty.

314

315 We acknowledge that lithostratigraphic units are not strictly chronologically equivalent. This is
316 where the strength of the current approach which describes the lithology comes into play. Note
317 the good correspondence between the predicted depth of formations from the polynomial fit of
318 the sample ages and lithological and slope changes observed in the dive (open red circles in
319 Figure 4). These lithological and morphological delineations would also be the key criteria in the

320 delineation of lithostratigraphic formations onshore. These changes are shown in red lines in
321 Figure 3.

322

323 A marked change in the section is observed at 2650 m (Figure 4.1). The slope above this depth is
324 talus with minimal rock exposure (Figure 3). Below this depth, the slope has several intervals
325 with in-situ rock surfaces (Figure 3), one of which exhibits a prominent eroded channel (Figure
326 4.1). A sample of hard clay had been dated to latest Eocene (Priabonian), possibly earliest
327 Oligocene (Table 1, Figure 4.1) and is older than a sample taken from the upper San Sebastian
328 interval at a depth of 2352 m. A 274 m thick layer of possibly Eocene age, consisting of
329 claystone and calcareous and silicic volcanic sandstone, underlies the San Sebastian Formation
330 in borehole 4CPR, probably separated by an unconformity (Briggs, 1961). The bottom of the
331 Eocene (?) layer was not reached in borehole 4CPR. A thick (2125 m) Eocene age volcanoclastic
332 unit, separated by an unconformity from the overlying San Sebastian Formation, was
333 encountered in the Toa Baja borehole (Montgomery et al., 1991; Larue, 1991). It contains
334 volcanoclastic sandstone, marly pelagic limestone, and chert (Larue, 1991). Larue and Berrong
335 (1991) and van Gestel et al. (1998) extended the Eocene layer offshore by identifying a ≥ 1.5 s
336 thick seismic layer of continuous low-frequency reflectors. Van Gestel et al. (1998) suggested
337 that this section was deposited in a forearc basin environment with variable depths.

338

339 An abrupt transition from a moderately-sloped talus to an overlying layered and steep rock wall
340 is observed at a depth of 2315 m (Figures 3 and 4.3). The Oligocene San Sebastian Formation
341 was deposited in terrestrial, coastal, and shallow marine deposits and mostly comprises of
342 erodible silicic and volcanic sandstone, mudstone, and calcareous claystone (Ward et al., 2002,

343 and references therein). The overlying Lares Formation was deposited in an inner- to mid-
344 platform environment with carbonate and terrigenous deposits and small coral patches (Ward et
345 al., 2002). Ward et al. (2002) placed the boundary in the uppermost Chattian, close to the
346 Oligocene-Miocene boundary, which is predicted to be located at a depth range of 1920-2040 m
347 according to our polynomial fit (Figure 5). Seiglie and Moussa (1984) and Hubbard (1923)
348 suggested however, a Middle Oligocene age for this boundary, 27.4 and 28.1 Ma, respectively,
349 for the San Sebastian-Lares boundary. These ages fall within the predicted ages for a depth of
350 2315 m in Figure 5. We, therefore, suggest that the transition between the San Sebastian
351 Formation and Lares Limestone occurred in the Middle Oligocene and not in the Late Oligocene.
352

353 We placed the boundary between the Lares Limestone and Cibao Formation along a ledge and an
354 apparent unconformity at a depth of ~2018 m (Figures 3, 4.6). Our identified top Lares
355 Formation is a ~50 m layered section with a steep slope overlying a 50 m talus of lower slope
356 angle. A similar configuration is described by Monroe (1980) from outcrops, namely
357 fossiliferous limestone overlying chalk and calcareous clay, and in 4CPR borehole, where a ~80
358 m of calcarenite and dense limestone overlies ~50 m of marl and calcareous claystone (Briggs,
359 1961).

360

361 We placed the boundary between the Cibao and Aguada Formations at 1854 m where high-
362 frequency layering (20-30 cm thick) below changes to a massive rock face above (Figure 4.7).
363 The contact is conformable, similar to observations in drill holes on land (Ward et al., 2002). The
364 Cibao Formation along our dive transect is divided into three general units: The lower unit is a
365 140 m section of steep slope with ~1 m thick layers, bottomed by talus and lower slope rock

366 surface (Figure 4.6). The 40 m middle unit is talus. The top 65 m thick layer is hard rock with
367 thin layering (Figure 4.7). Our interpretation of this interval as belonging to Cibao Formation is
368 based on similar lithologic variations reported in 4CPR borehole for this formation: a 155 m
369 lower unit of calcarenite and dense limestone, whose bottom 20 m have claystone layers, a 50 m
370 middle unit of claystone and a 100 m top unit of calcarenite and dense limestone (Briggs, 1961).

371
372 The boundary between Aguada Formation and Aymamón Limestone is placed at a depth of 1832
373 m where a ledge is observed (Figure 4.8). Based on outcrops studies, Meyerhoff et al. (1983)
374 suggested that the boundary is an erosional unconformity, while Monroe (1980) described the
375 boundary as an abrupt change from thin-bedded layers of Aguada to thicker bedded layers of
376 Aymamón. The boundary is less clear in 4CPR borehole (Briggs, 1961). The overlying section
377 consists of a steep smooth rock surface with dark bands, representing perhaps equivalent
378 dolomitic-rich layers of the Aymamón Limestone in the borehole (Figures 4.8, 4.9).

379
380 Sample 033 at a depth of 1762 m and dated at 13-13.5 Ma, is located at an unconformity between
381 a massive and steep rock wall and a sediment-covered plain (Figure 4.9). An unconformity on
382 top of Aymamón Limestone, a massive calcarenite and calcitic dolomite layer encountered in
383 4CPR borehole (Briggs, 1961), is dated at a similar age (12.5 Ma) (Table 2). Monroe (1980) and
384 Meyerhoff et al. (1983) suggested that the unconformity is a karst surface. The unconformity
385 represents a hiatus of ~6 Myr (12.5 to 6.6 Ma) (Table 2) underlying the Late Miocene-Early
386 Pliocene Quebradillas Limestone (Ward et al., 2002).

387

388 Using our polynomial interpolation, the expected depth at 6.6 Ma, the age of the base of
389 Quebradillas Limestone outcrops on land, is 1674 m (Figure 5) or 100 m below the top of the
390 dive transect. At this depth, rocky benches with patina interspersed with short sandy slopes
391 above, change abruptly to a 35 m high steep massive rock without patina below (Figure 4.10).
392 Monroe (1980) estimates the total thickness of the Quebradillas Limestone units on land to be
393 about 100 m (Ward et al., 2002). Previous authors (Ward et al., 2002; Seiglie and Moussa, 1984;
394 Monroe, 1980; Meyerhoff, 1975) estimated the unconformity between the Aymamón and
395 Quebradillas Limestones on land to span several million years. If 1674 m is the bottom of
396 Quebradillas Limestone, it leaves the dive interval between 1762 (the prominent unconformity
397 on top of Aymamón Limestone) and 1674 m as a section with no known equivalence in outcrops
398 or in boreholes on land. We therefore labeled this interval as ‘undefined’ (Figure 3 and Figure 5).

399

400 **DISCUSSION**

401 **Comparison to 4CPR borehole and lateral variation in the carbonate shelf.**

402 Two continuous borehole sections bottoming in Eocene (Toa Baja borehole, Larue, 1991) and
403 Oligocene (4CPR, Briggs, 1961) were recovered on land close to the coastline (see Figure 1B for
404 location). Thickness variations between these two holes are large, as described below. The Toa
405 Baja borehole penetrated 585 m of fossiliferous Oligocene and Miocene limestone, sandstone,
406 and shale. Quebradillas Limestone rocks were not encountered in this borehole (Montgomery et
407 al., 1991). The section below 585 m is dated biostratigraphically as Eocene, but the ages of the
408 lower half of the Eocene section overlap with the ages of the top half (Montgomery et al., 1991).
409 The shallowest depth in which the oldest date is encountered, is 885 m. We used this depth as a
410 data point in Figure 6. The base of Oligocene San Sebastian Formation in 4CPR borehole is at a

411 depth of 1686 m. The bottom of the underlying Eocene (?) strata was not reached at the
412 maximum drilling depth of 2145 m (Briggs, 1961).

413

414 Briggs (1961) interpreted the Aymamón Limestone to reach the top of the borehole, implying
415 that Quebradillas Limestone was missing. Later evaluation of the foraminifera in the borehole
416 suggested, however, that the top 120-170 m part of the borehole belong to the Quebradillas
417 Limestone (Moussa et al., 1987). The depth uncertainty is due to the lack of cuttings recovery
418 between depths of 120-170 m (Briggs, 1961). Quebradillas Limestone outcrops on land reach a
419 maximum thickness of 110 m (van Gestel et al., 1998). We plotted a 120 m thick Quebradillas
420 Limestone in 4CPR borehole (Figure 6). We assumed that the age of the Lares Limestone -San
421 Sebastian formation boundary in both Toa Baja and 4CPR boreholes is 27.4 Ma (Seiglie and
422 Moussa, 1984), similar to Figure 5.

423

424 With the above age modifications to the data points, we can fit the data points for the formation
425 boundaries in boreholes 4CPR and Tao Baja using a 2nd order polynomial fit (Figure 6). The
426 shapes of the depth vs. age for all the curves indicate continuous accumulation within the
427 resolution of the data. Fluctuations in accumulation rates on smaller time scales are expected, for
428 example, Seiglie and Moussa (1984) proposed that global transgressive-regressive sedimentation
429 cycles dominated the paleo-depth deposition of the latest Oligocene to Pliocene strata. The
430 accumulation rate for Toa Baja borehole is relatively constant since the Eocene, but the
431 accumulation rate in the dive site and in 4CPR borehole decrease upward towards the present.
432 The decrease is most pronounced since the early Miocene in the dive site and may be the result

433 of a larger distance of the dive site from the paleo-shore as carbonate sedimentation rate
434 decreases with depth (Sultana et al., 2022).

435

436 **Using seismic profiles to spatially and vertically extend the dive interpretation**

437 Dive observations along vertical cliffs can serve as a lower cost alternative to drilling boreholes
438 for regional interpretation of seismic profiles. We extrapolate the dive results regionally using
439 nearby MCS profile EW9501-1289, SCS profile EW9605-P-31, and high-resolution MCS profile
440 Pelican Line 47 (Figure 7). The formation thicknesses from the dive observations were converted
441 to travel time using the seismic velocities in Table 3. These velocities are approximated from the
442 published synthetic seismogram of Toa Baja borehole, constructed by Anderson (1991, their
443 Figure 2) from their density and velocity logs. There are no other published seismic velocities for
444 the sedimentary section in northern Puerto Rico.

445

446 Three reflections can be interpreted in nearby seismic lines. The yellow reflector ~ 0.2 s below
447 seafloor (bsf) is probably the unconformity at the top of Aymamón Limestone, identified in the
448 dive at a depth of 1762 m (Figure 4.9). The red reflector at ~ 0.72 s below the yellow reflector is
449 probably the unconformity separating the San Sebastian Formation from the underlying Eocene
450 forearc sediments at a depth of 2650 m (Figure 4.1). An unconformity separating the Eocene
451 section from the overlying San Sebastian Formation, was encountered in Toa Baja borehole
452 (Montgomery et al., 1991; Larue, 1991). The blue reflector is likely the boundary between the
453 Eocene forearc sediments and the underlying basement. Using an average velocity of 4450 m/s,
454 the thickness of the Eocene layer is 860 m in Line 1289 and 1120 m in Line P-31 (Figure 7). Our
455 dives, which extended 1277 m below the presumed San Sebastian – Eocene boundary at a depth

456 of 2650 m, did not identify the Eocene-basement boundary. Note, however, that the thickness of
457 the Eocene layer has been observed to change rapidly on seismic lines north of Puerto Rico
458 (Mondziel et al., 2010; van Gestel et al., 1998).

459

460 A separate ROV dive, EX1502-04, collected a video stream along a transect between depths of
461 3167-3927 m, leaving a gap of 300 m of unvisited slope from the overlying and above described
462 NA035-1300 dive (Figure 3). Rock samples were not collected during dive EX1502-04, and
463 therefore, the ages of the outcropping units are known. Visually, most of the slope is covered by
464 talus with occasional fields of strewn stones and blocks. However, two major steep faces of
465 outcrops are visible at depth intervals of 3247-3396 m (149 m; Figure 8.1-8.2) and 3717-3788 m
466 (81 m; Figure 8.3-8.4), and smaller ones were observed at depth intervals between 3603-3616 m
467 and 3572-3582 m. Some of the outcrops appear layered (e.g., Figure 8.2) and others are not
468 (Figure 8.1). Where layering is observed, their dips in dive EX1502-04 are variable (Figure 8.1
469 and 8.4) sometimes even within a few meters (Figure 8.3), in contrast to the dips observed in
470 NA035-1300 which are close to horizontal (Figures 4.3-4.12), sometimes exhibiting opposing
471 dip orientations (Figure 8.3). The volcanoclastic sequence in Toa Baja borehole comprises a
472 variety of lithologies including volcanoclastic sandstone, mafic lavas, intermediate lavas, tuffs,
473 epiclastic deposits and marly pelagic limestone. Based on the depth and the heterogenous
474 composition of the virtual outcrops, we interpret the observed outcrops in dive EX1502-04 to
475 represent the Eocene volcanoclastic sequence, deposited in a forearc basin. If this interpretation is
476 correct, the Eocene sequence here reaches a water depth of almost 4000 m, only 1000 m above
477 the floor of Mona Rift. The interpreted Eocene-basement boundary in nearby seismic lines
478 EW9501-1289 and EW9605-P-3 is at approximate depth of 3510-3770 m, based on the velocity

479 (Table 3) and two-way travel time of the Eocene interval (Figure 7B, C). The Eocene thickness
480 was likely deposited at much shallower depths and attained its great depth by the post mid-
481 Pliocene tilting, which at this location amounted to 1560 m (Figures 4.12 and 5). After correcting
482 for the tilt, the interpreted depth of the Eocene sequence from the ROV dive, ~2500 m, would be
483 similar the depth of the Eocene section encountered in the Toa Baja borehole onshore, ~2700 m.

484

485 **Style and timing of the opening of Mona Rift**

486 The western edge of Mona Rift is a curved steep wall enclosing a broad triangular area with
487 bathymetric lineaments at depths of 3000-4000 m above the relatively flat floor of the rift
488 (Figure 9 map). Where crossed by seismic lines, these lineaments line up with boundaries of
489 tilted fault blocks (Figure 9A, B). The blocks are tilted to the east but appear to be internally
490 competent. We interpret these blocks to be down-dropped blocks of the reflective sedimentary
491 section observed in Figure 6. The normal fault bounds the tilted blocks dip to the west (Figure
492 9A) and perhaps soles into a major east-dipping curved normal fault (Figure 9B). Evidence for
493 the sense of motion on this major east-dipping fault can be deduced from the observed “pull-
494 down” of seismic reflectors at the west wall (Figure 7). The fault system on the west side faces a
495 semi-linear steep slope along the eastern wall of the rift (Figure 9 map), which Mondziel et al.
496 (2010) interpreted to be the main fault along which Mona Rift extension took place.

497

498 Mondziel et al. (2010) proposed that opening of Mona Rift started in mid-Oligocene because
499 they interpreted the thickness difference of the Mid-Oligocene-to Pliocene section across Mona
500 Rift (~1.3 s to the west and 0.6 s to the east; Figure 9B) to arise from differential sediment
501 accumulation between the footwall and hanging wall during motion on a normal fault along the

502 east side of the rift. Such geometry predicts a gradually thickening sedimentary wedge on the
503 hanging wall eastward toward the fault. They explained the absence of the eastward thickening
504 to be the results of a very steep fault. We contend that the thickness variations across the rift
505 existed prior to extension. For example, Larue et al. (1998) mapped several basement highs north
506 of Puerto Rico including Guajataca High close to the eastern wall of Mona Rift. Similarly, van
507 Gestel et al. (1998) mapped variations in the Oligocene to Miocene sequence north of the island
508 with a thinner section close to the eastern wall of Mona Rift toward the fault. Similar large
509 thickness variations are also observed onshore (Ward et al., 2002). Furthermore, figure 9B shows
510 that sedimentary section within the rift basin is slightly thinner than under the west wall.

511

512 We suggest therefore that Mona Rift opened after the deposition of the latest sediments in the
513 mid-Pliocene, probably as part of the large-scale tilting of the carbonate platform and the
514 foundering of the Puerto Rico Trench (ten Brink, 2005). Younger sediments appear to partially
515 fill the wedges between the internally competent tilted blocks, and some of these sediments are
516 deformed (Figure 9A). Thickness variations in the sediment fill of the rift floor above the
517 carbonate sequence also appear to adjust to the rift floor subsidence (Figure 9A, B).

518

519 **The reason for absence of Fe-Mn crust on significant portions of the dive transect**

520 A 183-m interval of the section between depths of 1920 m and 1674 m (Figure 4.7-4.9, 4.10) as
521 well as additional smaller intervals of tens of meters deeper in the section (between 1964-1973
522 m), are mostly devoid of patina or Fe-Mn crust. The lack of patina over such a large interval can
523 be attributed either to a high slip rate on the secondary antithetic fault (Figure 9B), or to one or
524 more landslides, or to the morphology of the outcrop. Assuming that patina is being developed

525 over 10^5 - 10^6 yr (Conrad et al., 2017), the slip rate should be faster than 1.5 mm/yr. Such a high
526 rate of movement on a secondary fault is expected to generate earthquakes with significant
527 magnitude every few hundreds of years. Additional antithetic faults, not identified in the seismic
528 profiles would generate the other intervals of missing patina.

529

530 An alternative explanation is that the exposed sections lacking patina and the down-tilted blocks
531 were formed by large blocks sliding into the deepening rift. A single landslide can detach blocks
532 that are tens to 100s of meter thick from the existing walls. Chasms in the carbonate platform,
533 similar to the one observed farther west on the platform, and similar to chasms observed at the
534 edge of the carbonate platform north of Puerto Rico (ten Brink et al., 2006) could nucleate
535 landslides in the upper part of the carbonate platform. However, it is unclear whether the fault
536 blocks shown in Figure 9A and B at depths of 3000-4800 m were transported there by landslides.
537 At least some of the blocks appear to retain their internal layering and thickness across this area
538 and continue under the flat floor of Mona Rift.

539

540 The third possibility is associated with cliff morphology. Patina is lacking where the slope is
541 steep and the rock face is massive and smooth without alternating layers of different strength,
542 and perhaps lithology (Figure 3B, 4.8, 4.9). Smooth rock surface may be prone to continuous
543 erosion of the surface by currents and gravity inhibiting patina growth. A recent investigation of
544 the relationship between the degree of patina erosion and the distribution of hydrographic and
545 topographic controls in an eastern Atlantic seamount hinted at the presence of patina erosion
546 above current speed of 0.2 m/s, although relation is complex (Yeo et al., 2019). Current speed is

547 generally higher on a smooth surface compared to a rough one due to the reduction in the surface
548 friction drag. We thus, favor this last explanation for the lack of patina.

549

550 **CONCLUSIONS**

551 We extend traditional concepts of field geology to great ocean depths by using photogrammetry
552 to construct virtual outcrops from a string of overlapping video frames collected by remotely
553 operated vehicles (ROV). The imagery was collected along dive transects on the west wall of
554 Mona Rift between water depths of 1560 and 3927 m. Mona Rift is a deep and narrow chasm
555 NW of Puerto Rico and is surrounded by carbonate platform. This platform also extends
556 eastward offshore for 150 km and onshore into the north coast of Puerto Rico and. There are no
557 drillholes offshore and tying seismic lines across the shoreline is problematic. Here, we describe
558 the process and limitations of constructing a virtual outcrop and describe our observations. We
559 constrain stratigraphy and age of the virtual outcrop using 7 ROV grab samples. Our stratigraphy
560 and assigned ages agree for the most part with deep boreholes and outcrops on land. We
561 identified, however, a 100 m thick section, which on land is represented by an unconformity. Our
562 stratigraphic interpretation indicates lateral variations in formation thicknesses from land to
563 offshore and across to nearby marine seismic profiles. It establishes a cross-section that can be
564 used for additional sampling of the basin geology, specifically, the layering of the carbonate
565 platform, which may be controlled by global transgressive-regressive sedimentation cycles
566 (Seiglie and Moussa, 1984). Our analysis and correlation with adjacent seismic profiles also
567 suggest that, unlike previous suggestions, Mona Rift was formed only since mid-Pliocene.

568

569 Large amounts of video images have been collected in deep water by various organizations for
570 outreach, educational, and other purposes. The wealth of available opportunistic imaging can be
571 used in the right locations to construct virtual outcrops. Coupled with collected rock samples,
572 ROV imagery, thus, offers a cheaper alternative to drilling boreholes offshore and to ground-
573 truthing marine seismic profiles.

574

575 **Acknowledgments**

576 We are indebted to Dr. Robert Ballard and Ocean Exploration Trust and to NOAA's Ocean
577 Exploration Program for the use of their ships, ROVs, and technical expertise. We thank Dwight
578 Coleman, Amanda Demopoulos, Nicole Reineault, Brian Kennedy, Mike Cheadle, Andrea
579 Quattrini and the rest of the onboard and remote participants in cruises NA-035 and EX1502.
580 Bill Danforth helped with the initial processing steps. We thank Jerzey Blusztajn, WHOI for
581 measuring $^{87}\text{Sr}/^{86}\text{Sr}$ isotope ratio in four of the samples. Walter Barnhardt and Robert Halley
582 reviewed an earlier version of the manuscript and offered many constructive suggestions. Videos
583 collected during the National Oceanic and Atmospheric Administration's (NOAA) Ocean
584 Exploration cruise EX1502 are available from NOAA's video archive portal
585 <https://www.ncei.noaa.gov/access/ocean-exploration/video/> (last accessed March 2020). Rock
586 samples are available at <https://web.uri.edu/gso/research/marine-geologicalsamples-laboratory/>
587 (last accessed March 2020). Ocean Exploration Trust videos from expedition NA-035 are
588 available upon request at <https://nautiluslive.org/science/data-management> (last accessed March
589 2020). SCS line EW9605 P47 is available at [https://www.marine-
590 geo.org/tools/search/Files.php?data_set_uid=21919#datasets](https://www.marine-geo.org/tools/search/Files.php?data_set_uid=21919#datasets). MCS line EW9501 1289 is
591 available at https://www.marine-geo.org/tools/search/Files.php?data_set_uid=3752. MCS line P-

592 31 is available at <https://walrus.wr.usgs.gov/namss/survey/p-30-06-cb/>. Any use of trade, firm, or
593 product names is for descriptive purposes only and does not imply endorsement by the U.S.
594 Government.

595

596 **References cited**

597 Anderson, R.N., 1991, Geophysical logs from the Toa Baja scientific drillhole, Puerto Rico.
598 Geophysical Research Letters, v. 18, p.497-500.

599 Andrews, B.D., U.S. ten Brink, W.W. Danforth, J.D. Chaytor, J-L Granja-Bruna, P. Llanes
600 Estrada, and A. Carbo-Gorosobel, 2014. Bathymetric terrain model of the Puerto Rico Trench
601 and Northeast Caribbean for marine geological investigations, OFR 2013-1125.

602 <https://pubs.usgs.gov/of/2013/1125/>

603 Backman, J., Raffi, I., Rio, D., Fornaciari, E., Alike, P. 2012, Biozonation and biochronology of
604 Miocene through Pleistocene calcareous nannofossils from low and middle latitudes.
605 Newsletters on Stratigraphy, v. 45, p. 221–244.

606 Bell, K.L.C., M.L. Brennan, and N.A. Raineault, eds. 2014. New frontiers in ocean
607 exploration: The E/V *Nautilus* 2013 Gulf of Mexico and Caribbean field
608 season. *Oceanography* v. 27(1), supplement, 52 pp.

609 <https://doi.org/10.5670/oceanog.2014.supplement.01>.

610 Briggs, R.P., 1961, Geology of Kewanec Interamerican Oil Company test well number 4CPR,
611 northern Puerto Rico, in Oil and Gas possibilities of northern Puerto Rico: San Juan, Puerto
612 Rico Mining Commission, p. 1-23.

613 Conrad, T., Hein, J.R., A. Paytan, A., and Clague, D. A., 2017, Formation of Fe-Mn crusts
614 within a continental margin environment, *Ore Geology Review*, v. 87, p. 25–40.

- 615 Heezen, B.C., Nesteroff, W.D., Rawson, M. and Freeman-Lynde, R.P., 1985, Visual evidence
616 for subduction in the western Puerto Rico trench. In Symposium géodynamique des Caraïbes,
617 p. 287-304.
- 618 Hubbard, B. 1923, The geology of the Lares district, Porto Rico: N. Y. Acad. Sci., Sci. Survey of
619 Porto Rico and the Virgin Islands, v. 2, pt. 1, p. 1-115
- 620 Jakuba, M.V., Kinsey, J.C., Yoerger, D.R., Camilli, R., Murphy, C.A., Steinberg, D. and Bender,
621 A., 2011, September. Exploration of the Gulf of Mexico oil spill with the sentry autonomous
622 underwater vehicle. In Proceedings of the International Conference on Intelligent Robots and
623 Systems (IROS) Workshop on Robotics for Environmental Monitoring (WREM), San
624 Francisco, CA, USA p. 25-30.
- 625 Jolly, W.T., Lidiak, E.G. and Dickin, A.P., 2008, The case for persistent southwest-dipping
626 Cretaceous convergence in the northeast Antilles: Geochemistry, melting models, and tectonic
627 implications. Geological Society of America Bulletin, v. 120, p.1036-1052.
- 628 Kennedy, B.R.C., Cantwell, K., Sowers, D., Quattrini, A.M., Cheadle, M.J., L. and McKenna, L.,
629 2015. EX1502L3 Expedition Report- Oceana Profundo 2015: Exploring Puerto Rico's
630 Seamounts, Trenches, and Troughs. Office of Ocean Exploration and Research, Office of
631 Oceanic & Atmospheric Research, NOAA, Silver Spring, MD 20910. OER Expedition Rep.
632 2015-02-03, 93 p. doi:10.7289/V5NG4NM8
- 633 Larue, D.K., 1991, The Toa Baja Drilling Project, Puerto Rico: Scientific drilling into a non-
634 volcanic island arc massif. Geophysical Research Letters, v. 18, p.489-492.
- 635 Larue, D.K., 1994, Puerto Rico and the Virgin Islands. Caribbean geology, an introduction, in
636 Donovan, S.K., and Jackson, T.A., Kingston, UWIPA, p.151-165.

- 637 Larue, D.K. and Berrong, B., 1991, Cross section through the Toa Baja Drillsite: Evidence for
638 northward change in Late Eocene deformation intensity. *Geophysical Research Letters*, v. 18,
639 p.561-564.
- 640 Larue, D.K., Torrini, R., Smith, A.L. and Joyce, J., 1998, North Coast Tertiary basin of Puerto
641 Rico: From arc basin to carbonate platform to arc-massif slope. In: Lidiak, E.G., and Larue,
642 D.K., eds. *Tectonics and geochemistry of the northeastern Caribbean*. Boulder, Geological
643 Society of America Special Paper 322, p. 155-176.
- 644 Lee, Z., Wei, J., Voss, K., Lewis, M., Bricaud, A. and Huot, Y., 2015, Hyperspectral absorption
645 coefficient of “pure” seawater in the range of 350–550 nm inverted from remote sensing
646 reflectance. *Applied Optics*, v. 4, p.546-558.
- 647 López-Venegas, A.M., ten Brink, U.S. and Geist, E.L., 2008, Submarine landslide as the source
648 for the October 11, 1918 Mona Passage tsunami: Observations and modeling. *Marine
649 Geology*, v. 254, p.35-46.
- 650 Marx, D., Nelson, M., Chang, E., Gillespie, W., Putney, A. and Warman, K., 2000, August. An
651 introduction to synthetic aperture sonar. In *Proceedings of the Tenth IEEE Workshop on
652 Statistical Signal and Array Processing (Cat. No. 00TH8496)*, p. 717-721. IEEE.
- 653 Meyerhoff, A.A., Krieg, E. and Closs, J., 1983, Petroleum potential of Puerto Rico. *Oil & gas
654 journal*, v. 81, p.113-120
- 655 Meyerhoff, H.A., 1975, Stratigraphy and petroleum possibilities of middle Tertiary rocks in
656 Puerto Rico: discussion. *AAPG Bulletin*, v. 59, p.169-172.
- 657 Micallef, A., Le Bas, T.P., Huvenne, V.A., Blondel, P., Hühnerbach, V. and Deidun, A., 2012, A
658 multi-method approach for benthic habitat mapping of shallow coastal areas with high-
659 resolution multibeam data. *Continental Shelf Research*, v. 39, p.14-26.

- 660 Mondziel, S., Grindlay, N., Mann, P., Escalona, A. and Abrams, L., 2010, Morphology,
661 structure, and tectonic evolution of the Mona canyon (northern Mona passage) from
662 multibeam bathymetry, side-scan sonar, and seismic reflection profiles. *Tectonics*, v. 29, no.
663 2.
- 664 Monroe, W.H., 1980, *Geology of the middle Tertiary formations of Puerto Rico*, Geological
665 Survey Professional Paper No. 953. Washington, US Government Printing Office.
- 666 Montgomery, H., Robinson, E., Saunders, J. and Van den Bold, W., 1991, Paleontology of the
667 Toa Baja# 1 Well, Puerto Rico. *Geophysical Research Letters*, v. 18, p.509-512.
- 668 Moussa, M.T., Seiglie, G.A., Meyerhoff, A.A. and Taner, I., 1987, The Quebradillas Limestone
669 (Miocene-Pliocene), northern Puerto Rico, and tectonics of the northeastern Caribbean
670 margin. *Geological Society of America Bulletin*, v. 99, p.427-439.
- 671 Pindell, J.L. and Kennan, L., 2009. Tectonic evolution of the Gulf of Mexico, Caribbean and
672 northern South America in the mantle reference frame: an update. Geological Society,
673 London, Special Publications, v. 328, p.1-55.
- 674 Pringle, J.K., Howell, J.A., Hodgetts, D., Westerman, A.R. and Hodgson, D.M., 2006. Virtual
675 outcrop models of petroleum reservoir analogues: a review of the current state-of-the-art. *First*
676 *Break*, v. 24, no. 3.
- 677 Román, Y.A., Pujols, E.J., Cavosie, A.J. and Stockli, D.F., 2021, Timing and magnitude of
678 progressive exhumation and deformation associated with Eocene arc-continent collision in the
679 NE Caribbean plate. *Geological Society of America Bulletin*, v. 133, p.1256-1266.
- 680 Seiglie, G.A. and Moussa, M.T., 1984, Late Oligocene-Pliocene transgressive-regressive cycles
681 of sedimentation in northwestern Puerto Rico, Schlee, J.S., ed., *Interregional unconformities*
682 *and hydrocarbon accumulation*, AAPG Memoir 36 p. 89-95.

683 Smith, A.L., Severin, K. and Larue, D.K., 1991, Stratigraphy, geochemistry and mineralogy of
684 Eocene rocks from the Toa Baja Drillhole. *Geophysical Research Letters*, v. 18, p.521-524.

685 Squyres, S.W., Knoll, A.H., Arvidson, R.E., Ashley, J.W., Bell III, J.F., Calvin, W.M.,
686 Christensen, P.R., Clark, B.C., Cohen, B.A., de Souza Jr, P.A. and Edgar, L., 2009.
687 Exploration of Victoria crater by the Mars rover Opportunity. *Science*, v. 324, p.1058-1061.

688 Stakes, D. S., Perfit, M. R., Tivey, M. A., Caress, D. W., Ramirez, T. M., and Maher, N., 2006,
689 The Cleft revealed: Geologic, magnetic, and morphologic evidence for construction of upper
690 oceanic crust along the southern Juan de Fuca Ridge. *Geochemistry, Geophysics, Geosystems*,
691 v. 7, no. 4.

692 Styzen, M.J., 1997. Cascading Counts of Nannofossil Abundance. *Journal of Nannoplankton*
693 *Research*, v. 19, p. 49.

694 Sultana, D., Burgess, P. and Bosence, D., 2022, How do carbonate factories influence carbonate
695 platform morphology? Exploring production– transport interactions with numerical forward
696 modelling. *Sedimentology*, v. 69, p.372-393.

697 ten Brink, U., 2005. Vertical motions of the Puerto Rico Trench and Puerto Rico and their cause.
698 *Journal of Geophysical Research: Solid Earth*, v. 110, no. B06404.

699 ten Brink, U., Chaytor, J., Flores, C., Wei, Y., Detmer, S., Lucas, L., Andrews, B. and
700 Georgiopoulou, A., 2023. Seafloor Observations Eliminate a Landslide as the Source of the
701 1918 Puerto Rico Tsunami. *Bulletin of the Seismological Society of America*, v. 113, p.268-
702 280.

703 ten Brink, U., Danforth, W., Polloni, C., Andrews, B., Llanes Estrada, P., Smith, S., Parker, E.,
704 Uozumi, T., 2004. New seafloor map of the Puerto Rico trench helps assess earthquake and
705 tsunami hazards in the northwest Caribbean, *EOS, Transactions, American Geophysical*

- 706 Union, v., 85, no., 37, p. 349, 354.
- 707 ten Brink, U., Geist, E.L., Lynett, P., and B. Andrews, 2006. Submarine slides north of Puerto
708 Rico and their tsunami potential, in Caribbean Tsunami Hazard, edited by A. Mercado and P.
709 Liu, World Scientific Publishers, Singapore, p. 67-90.
- 710 ten Brink, U., Coleman, D.F., Chaytor, J.D, Demopoulos, A.W.J., Armstrong, R., Garcia-
711 Moliner, G., Raineault, N.A., Andrews, B.D., Chastain, R. Rodrigue, K., and Mercier-
712 Gingras, M., 2014, Earthquake, Landslide, and Tsunami Hazards and Benthic Biology in the
713 Greater Antilles, *Oceanography* 27, p. 34-35, 51-52.
- 714 van Gestel, J.P., Mann, P., Dolan, J.F. and Grindlay, N.R., 1998. Structure and tectonics of the
715 upper Cenozoic Puerto Rico-Virgin Islands carbonate platform as determined from seismic
716 reflection studies. *Journal of Geophysical Research: Solid Earth*, v. 103, p.30505-30530.
- 717 Ward W.C., Scharlach, R.A., and Hartley, J.R., 2002, Geology of the north coast ground-water
718 province of Puerto Rico, in Renken, R.A., Ward, W.C., Gill, I.P., Gómez-Gómez, F. and
719 Rodríguez-Martínez, J., Geology and hydrogeology of the Caribbean islands aquifer system of
720 the commonwealth of Puerto Rico and the US Virgin Islands. US Geological Survey
721 Professional Paper 1419, p. 45-139.
- 722 Waterman, A.S., Center, M.W., George, R.A., Vallette, N.S., Porter, A.F., Reilly, T.M.,
723 Roederer, R.V., Sarao, J.S., Schmieder, J., Fillon, R.H., 2017, Biostratigraphic Chart–Gulf
724 Basin, USA: Paleogene. www.paleodata.com.
- 725 Yeo, I.A., Howarth, S.A., Spearman, J., Cooper, A., Crossouard, N., Taylor, J., Turnbull, M. and
726 Murton, B.J., 2019, Distribution of and hydrographic controls on ferromanganese crusts:
727 Tropic Seamount, Atlantic. *Ore Geology Reviews*, v. 114, p.103131.

728 Young, J.R., Bown P.R., Lees J.A., 2022, Nannotax3 website. International Nannoplankton
 729 Association. Accessed Apr-May 2023. URL: www.mikrotax.org/Nannotax3.
 730 Zapp, A.D., Bergquist, H.R. and Thomas, C.R., 1948. Tertiary geology of the coastal plains of
 731 Puerto Rico. U.S. Geological Survey Oil and Gas Inventory Preliminary Map OM-85, scale
 732 1:60,000. (Reprinted 1950.)
 733

734 **Table 1:** Rock samples grabbed with the ROV arm during dive NA035-1300.

Name	Lat. (N)	Long. (W)	W.D (m)	Grab sample description	Age based on nano-fossil assemblage	Confidence
NA035-035	18°43.7704'	67°35.7461'	1634	Mn-coated rock from rockslide area on slope, flat rock. Clay under Mn coating	3.61 - 4 Ma, Early Pliocene, upper Zanclean	High
NA035-033	18°43.7474'	67°35.3881'	1762	Rocks broken from outcrop (2), carbonate, vigorous bubbling with HCl	13–13.5 Ma, Middle Miocene, lower Serravallian	High
NA035-032	18°43.816'	67°35.2445'	1987	Rock showing both manganese coating and fresh,	~20.6-20.8 Early Miocene Aquitanian/	High

				uncoated rock, weak HCl fizz, Hard clay rock in 2 pieces, subsamples	Burdigalian boundary	
NA035-031	18°43.8546'	67°35.2'	2087	Rock, about 30 cm, vigorous bubbling with HCl, clay on striking with hammer, carbonate	Late Oligocene, Chattian (28.1-23 Ma)	Moderate
NA035-030	18°43.9229'	67°35.0765'	2232	Small, round rock, >10cm, carbonate, Vigorous fizz with HCl. internal structure, stripes, and dark patches	mid-Oligocene, Rupelian/Chattian boundary (28Ma ± 1.5 Ma)	Moderate to low
NA035-029	18°43.9432'	67°37.0352'	2352	Football-shaped rock, round, long, carbonate	Early Oligocene, Rupelian (28.1- 33.9 Ma)	Moderate to low
NA035-027	18°44.1574'	67°34.6724'	2660	Mn-coated rock from steep slope	Early Oligocene; possibly as old as	Moderate

				ridge, ~10 cm, vigorous fizz in HCl, hard clay rock	Late Eocene, Priabonian (33.9- 37.8 Ma)	
--	--	--	--	--	---	--

735

736 **Table 2.** Formations and geologic periods after Ward et al. (2002) and their equivalent ages

737 (after Geologic Time scale).

Formation name	Age (in m.y.)	Comments
Quebradillas Limestone	6.6-3.3	Top - unconformity
Ayamamón Limestone	15.1-12.5	Top - unconformity
Aguada (Los Puertos) Formation	16.5-15.1	
Cibao Formation	22.2-16.5	
Lares Limestone	24.25*-22.2	
San Sebastian Formation	33.9-24.25*	

738 * Seiglie and Moussa (1984) and Hubbard (1923) ages for the Lares Limestone-San Sebastian

739 Formation boundary is close to or at Middle Oligocene (27.4 Ma and 28.1 Ma, respectively).

740

741 **Table 3.** Seismic velocities used to convert depth to time for seismic interpretation.

Toa Baja borehole*			Velocity used for seismic interpretation		
Borehole interval (m)	Average velocity (m/s)	Interpretation from Montgomery et al. (1991)	Our interpretation	Depth interval (m)	Velocity (m/s)

**			Quebradillas+Undefined	1560- 1762	2100
0-152	2170	Base Aymamón (151 m)			
152-274	2440				
274-594	2670	Base San Sebastian (579 m)	San Sebastian to Aymamón	1762- 2650	2450***
594-660	3500				
660-2228	4340	Eocene	Eocene	< 2650	4450
2228-2670	5290				

742 * Measured from the log shown in Figure 2 of Anderson (1991).

743 ** Quebradillas Limestone was not identified in Toa Baja borehole.

744 *** Meyerhoff et al. (1983) projected poor-quality industry seismic reflection profiles to
 745 borehole 4CPR and interpreted the sedimentary section to be the base of San Sebastian
 746 Formation at approximately 1.2-1.4 s. Briggs (1961) interpreted the depth of the base San
 747 Sebastian Formation at 1684 - 1700 m, which yields a velocity range of 2430-2830 m/s.

748

749

750

751 **Figure captions:**

752 **Figure 1.** (A) Location map of dives NA035-1300 and EX1502-04 at the western wall of Mona
 753 Rift. Red lines – Dive transects. Blue lines – Locations of nearby seismic lines mentioned in text.
 754 Grey lines – 100 m contour interval. Bathymetry is a combination of multibeam bathymetry

755 collected aboard the E/V Nautilus during dive NA035-1300 and regional data (Andrews et al.,
756 2013). (B) – Regional map showing Mona Rift, the Puerto Rico subduction zone and prominent
757 faults. Red line – Edge of the tilted carbonate platform. Bathymetry from Andrews et al. (2014).
758 (C) Schematic drawing of the ROV operation described in the text. (D) Simplified stratigraphy
759 of the area based on boreholes onshore (Ward et al., 2002).

760

761 **Figure 2.** Images of three samples used in the study. On the left are photos of the ROV arm
762 grabbing the rock samples from the outcrop and on the right, images of the corresponding rock
763 samples. Note the black patina on the side of the rock surface, which was exposed to seawater.

764

765 **Figure 3.** (A) Observed slope angle as a function of depth for dive NA035-1300. Green lines and
766 red circles on left of diagram – Depth ranges of dive images and sample depths shown in Figure
767 4 and Table 1. Filled colored squares on the right is outcrop description (see legend). Open
768 squares mark noteworthy features (see legend). Thin red lines – Interpreted formation boundaries
769 (see text). (B) Image examples of textural interpretation of the rock face.

770

771 **Figure 4.1-3.12.** Select composite slope images from dive NA035-1300 generated by the
772 Structure from Motion procedure described in the text. Thin black lines – Depth contours at 10 m
773 interval. Video images were taken within a distance of a few meters of the outcrops. Image width
774 is generally proportional to the distance on the images between the depth contours, because the
775 field of view is generally perpendicular to the page. Image width is typically a few meters wide,
776 where the ROV moved up along slope and wider where the ROV moved diagonally, laterally, or

777 looped around in place. Red circle – Location of ROV grab sample listed in Table 1. Depth
 778 ranges of images are shown as green lines in Figure 3.

779

780 **Figure 5.** Graph of sample depths vs. their age ranges (Blue dots). An average, minimum, and
 781 maximum polynomial (Dashed blue lines) were fit to the dated range of dive samples and
 782 bracket the general trend of accumulation rate. However, fluctuations in accumulation rates on
 783 smaller time scales are likely, due, for example to sea level variations (Seiglie and Moussa;
 784 1984). Dashed green lines – Ages of formation boundaries from Ward et al. (2002). Dashed
 785 yellow line – Lares Limestone-San Sebastian Formation boundary from Seiglie and Moussa
 786 (1984). Queb. – Quebradillas Limestone. Agua. – Aguada Formation. S&M age – Seiglie and
 787 Moussa (1984) age for the Lares Limestone-San Sebastian Formation boundary. Open circles –
 788 Depths of interpreted formation boundaries based on dive observations. Notes that with the
 789 exception of the top of the dive which is interpreted as top Quebradillas Limestone, all other
 790 formation boundaries fall within or close to the bracketed trend. The curve fits for the maximum
 791 and minimum sample ages are $y = -0.7194x^2 + 1.8039x - 1645.6$; $R^2 = 0.9579$, and $y = -$
 792 $0.9798x^2 + 2.6878x - 1630.5$; $R^2 = 0.9989$, respectively.

793

794 **Figure 6.** Comparison of inferred formation boundaries in the dive transect (Figure 5) with
 795 formation boundaries in deep boreholes 4CPR and Toa Baja on land. A 2nd order polynomial fits
 796 showing general accumulation trends were fit to all three data.

797

798 **Figure 7.** Comparison of dive interpretation to nearby seismic profiles. A, B, C – Seismic
 799 profiles shown in location map D. Yellow dashed lines - Interpreted unconformity above

800 Aymamón Limestone. Red dashed lines– interpreted San Sebastian Formation – Eocene
801 unconformity. Blue dashed lines - Interpreted Eocene – basement boundary. Vertical purple
802 lines– Calculated two-way travel time intervals to top Aymamón Limestone and bottom San
803 Sebastian Formation converted from the depths in dive observations using the velocities in Table
804 3. Q – Quebradillas Limestone; U –An interval with undefined formation (see text). Note the
805 good agreement between the unconformities and the interpreted travel-time thicknesses from the
806 dive observations.

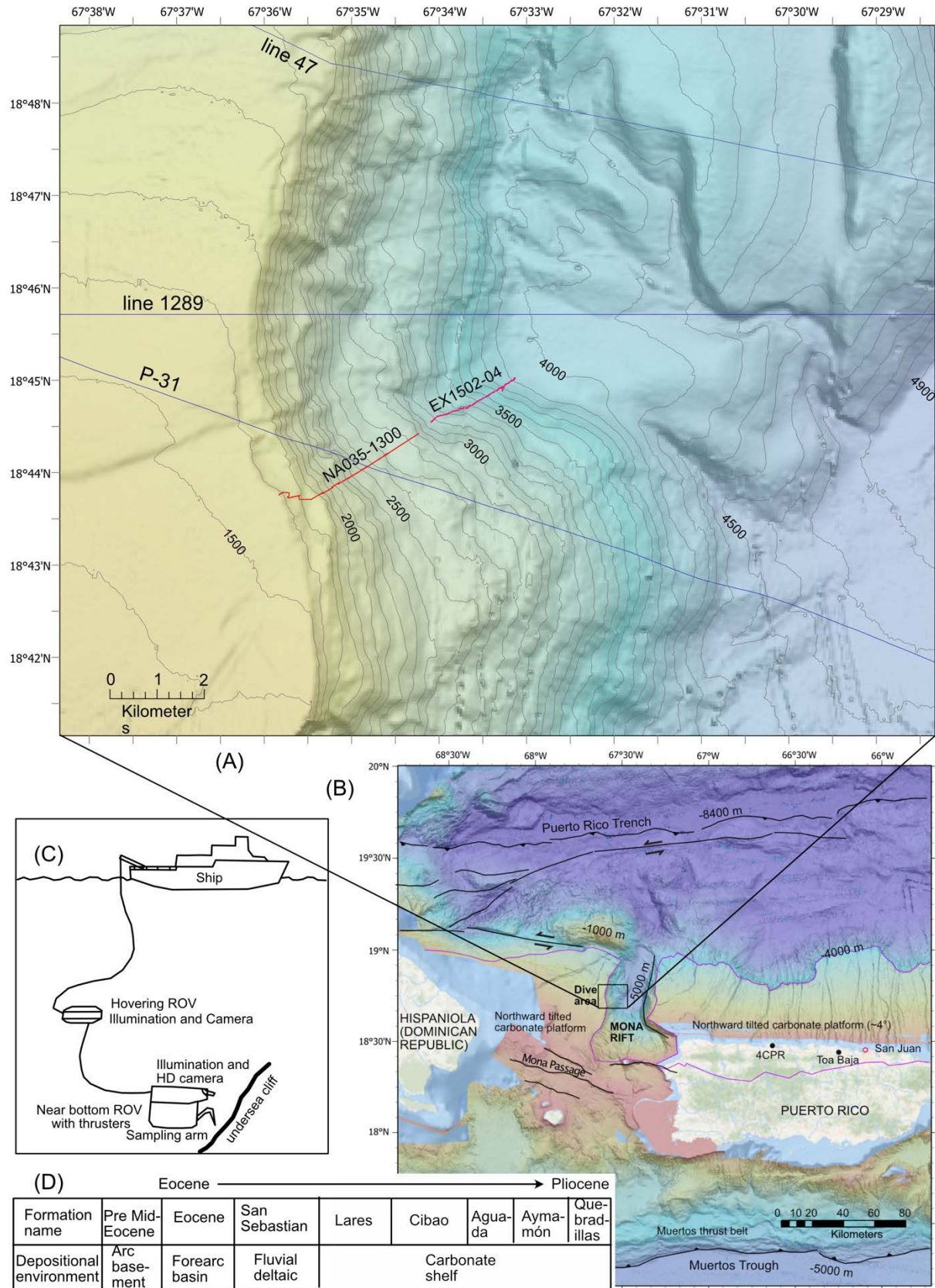
807

808 **Figure 8.1-8.4.** Select composite slope images from dive EX1502-04 generated by the Structure
809 from Motion procedure described in the text. Thin black lines – Depth contours at 5 m interval.
810 Note the absence of layering in Figure 8.1 and the opposing sense of weak layering between the
811 top and bottom of Figure 8.3.

812

813 **Figure 9 A, B, C:** Interpretation of broader and deeper extents of the seismic profiles shown in
814 Figure 7A, B, providing regional tectonic context. Dashed yellow lines in inset maps are
815 possible faults interpreted from the bathymetry and from crossing seismic lines. Green lines in A
816 and B – interpreted base infill overlying the Late Oligocene- mid-Pliocene carbonate platform.
817 The infill is likely related to the creation of Mona Rift. Blue lines in A, and B - Interpreted
818 Eocene – basement boundary. C – Location map of dive transects and seismic lines.

819



820

821 *Figure 1*



Sample NA035-035



Sample NA035-033



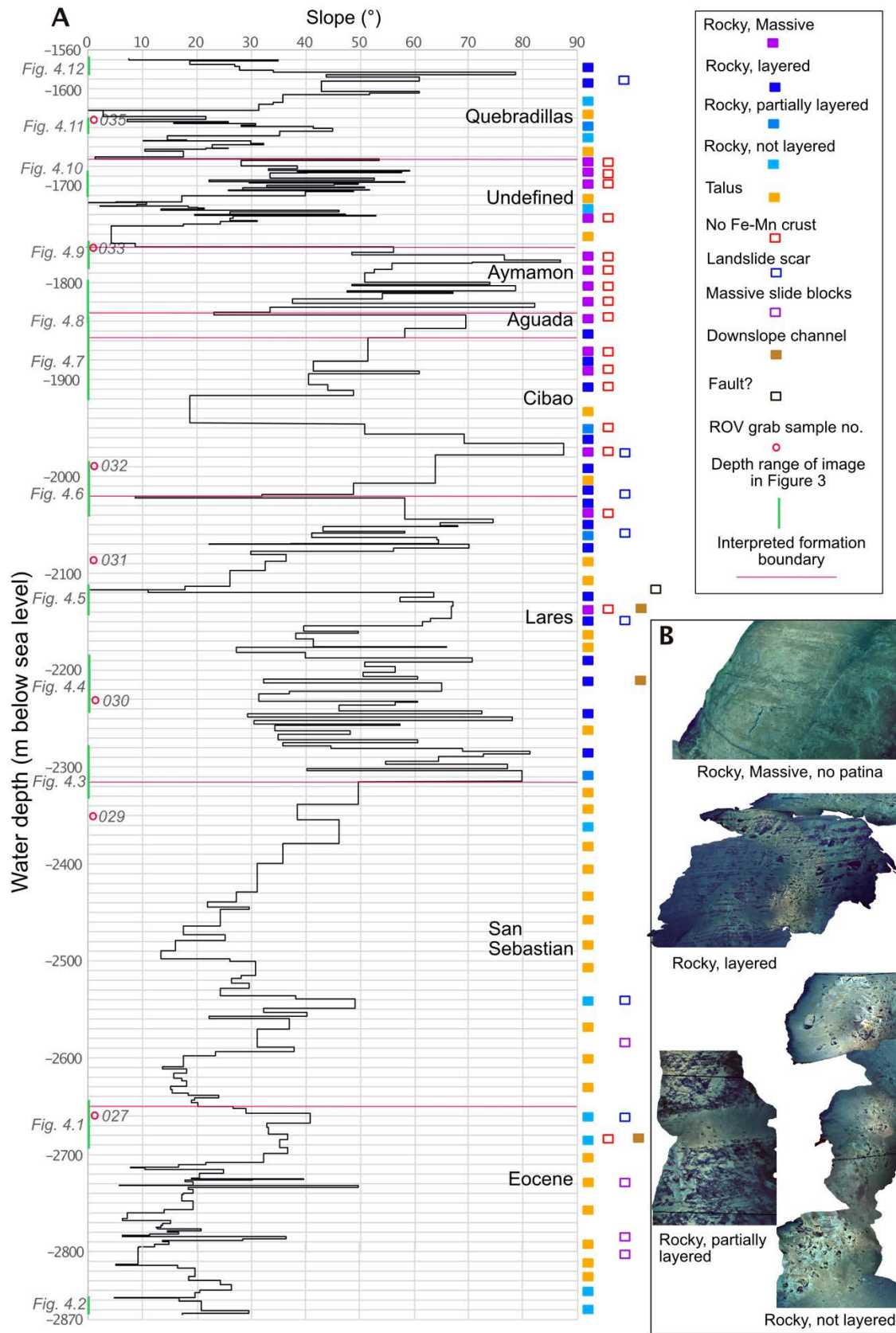
Sample NA035-027



822

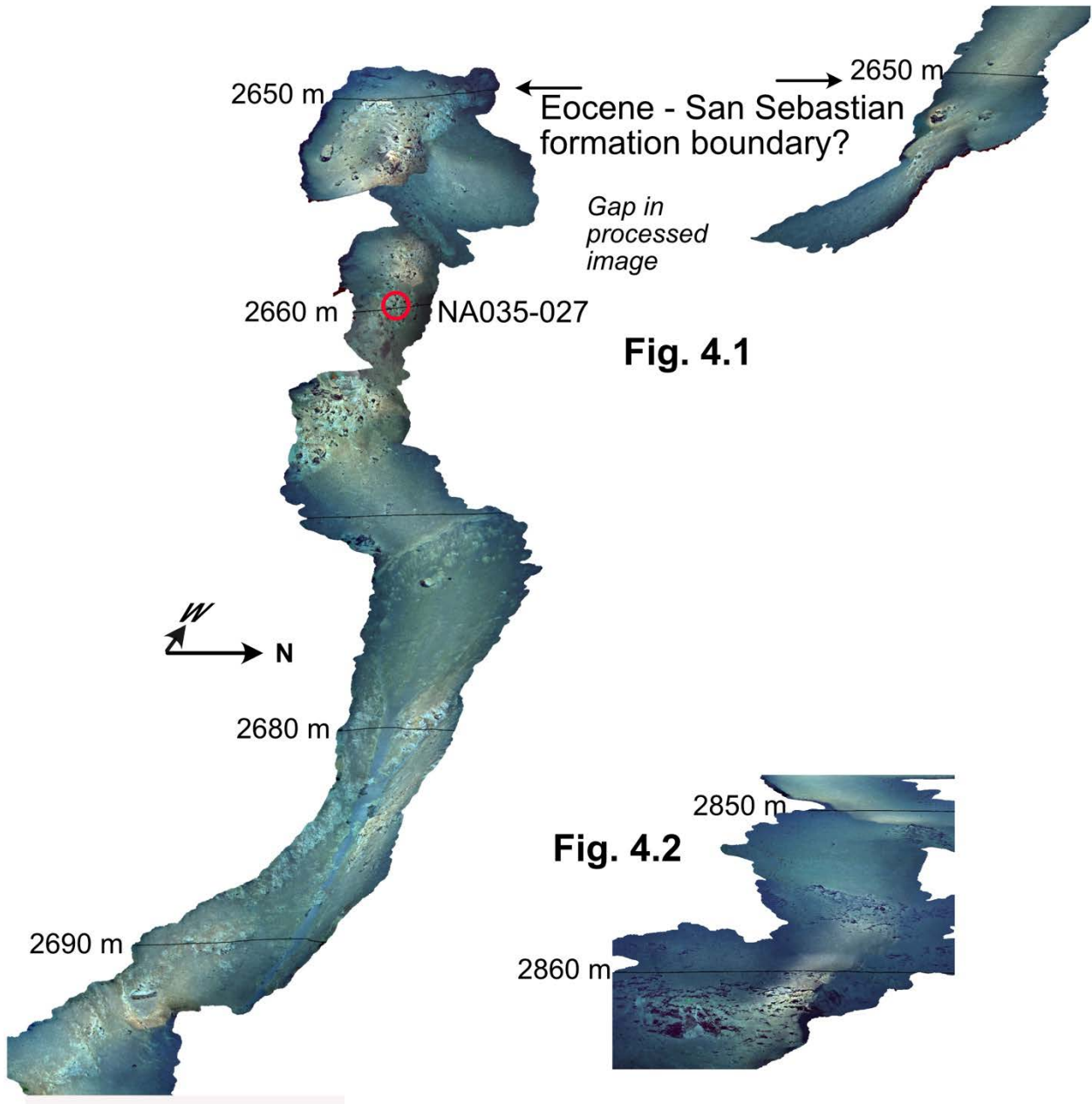
823 *Figure 2*

824

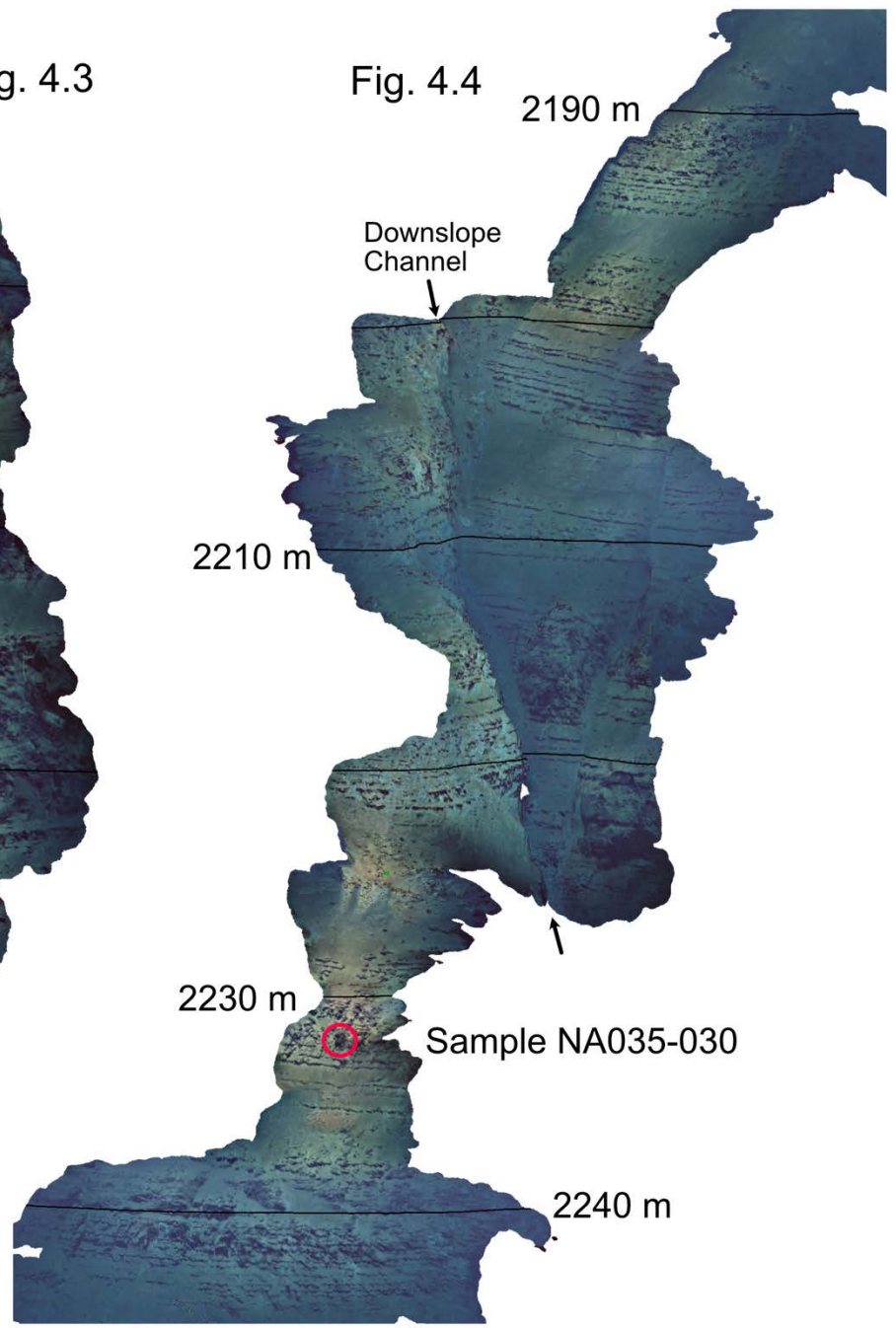


825

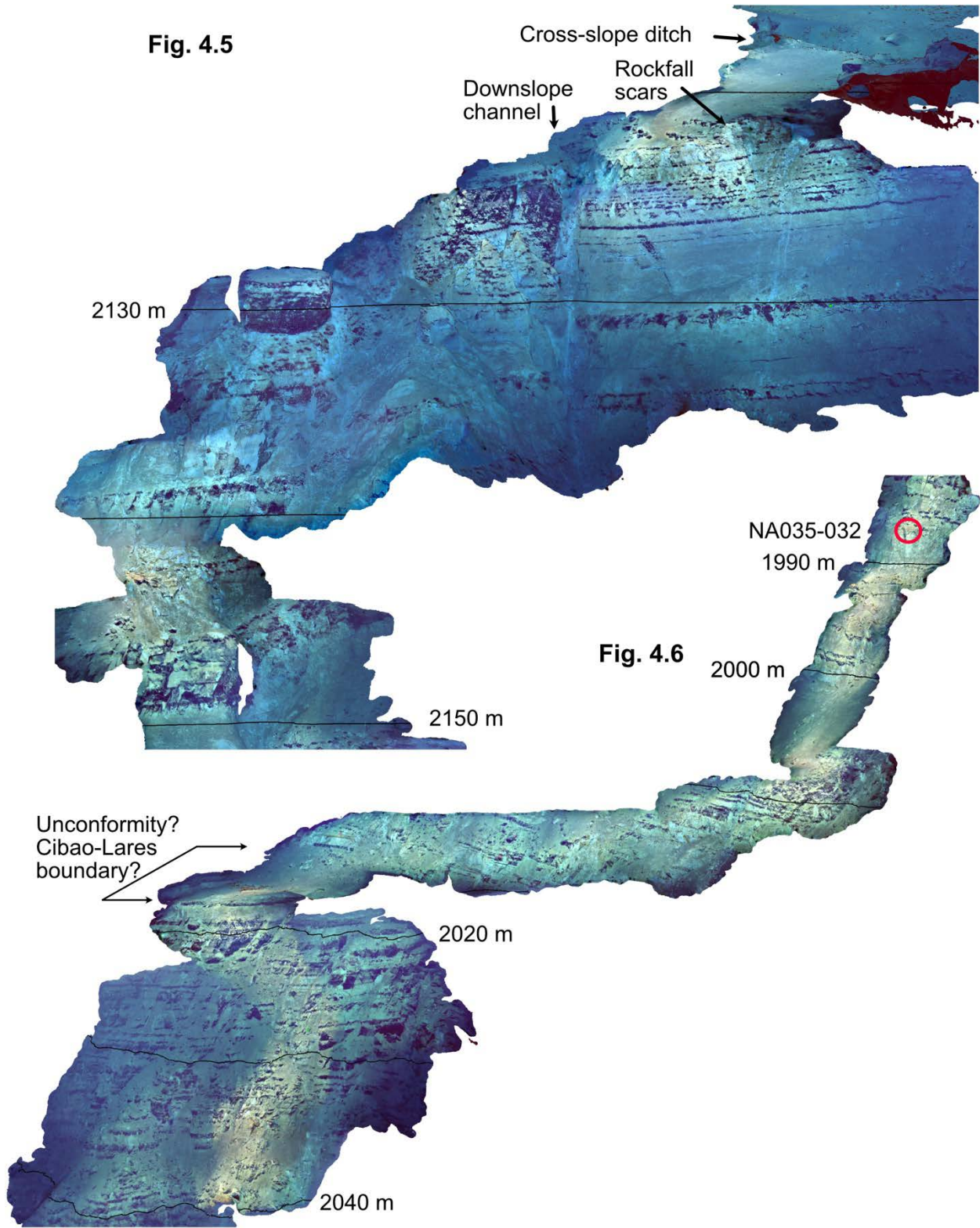
826 **Figure 3**



827

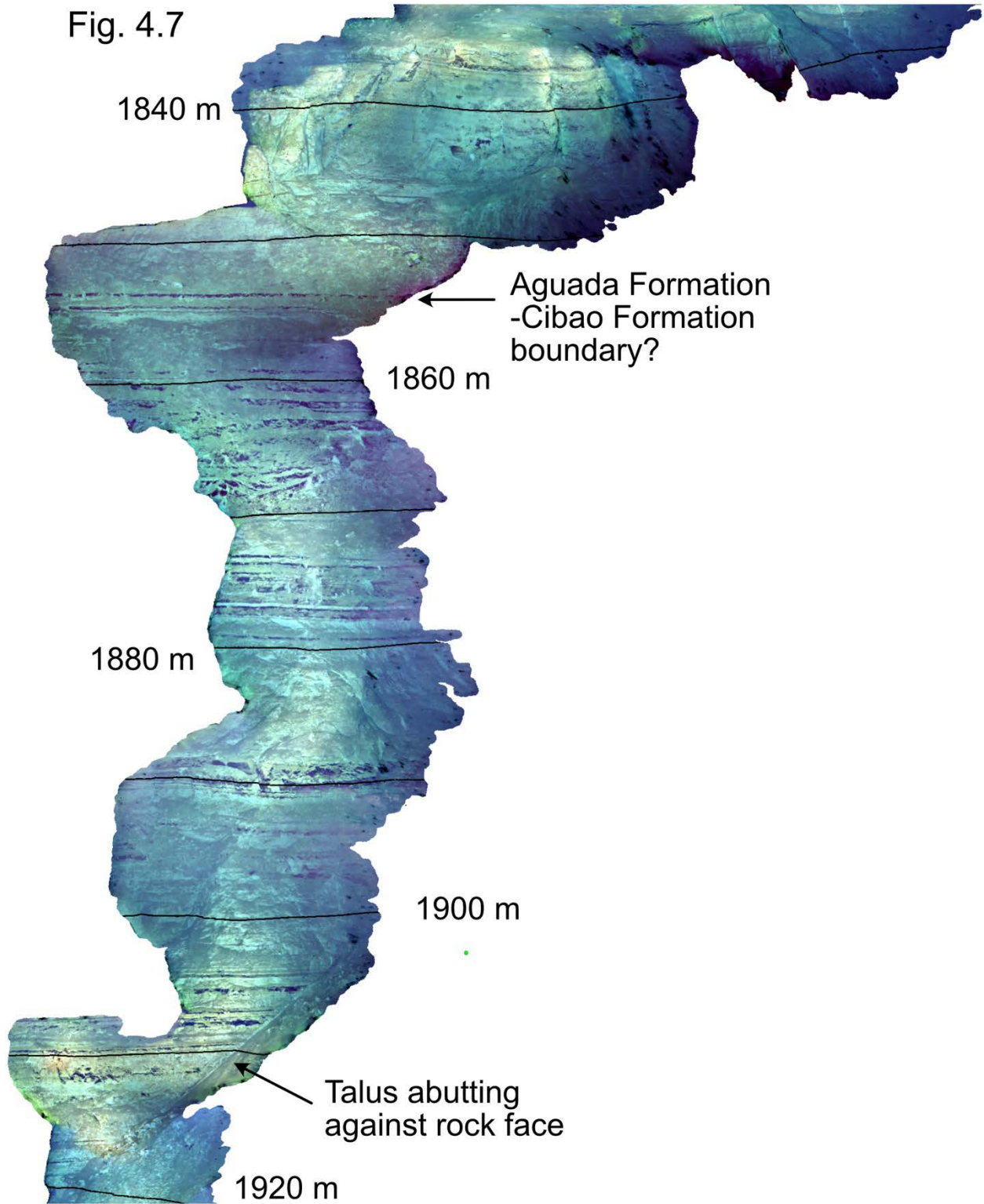


828
829

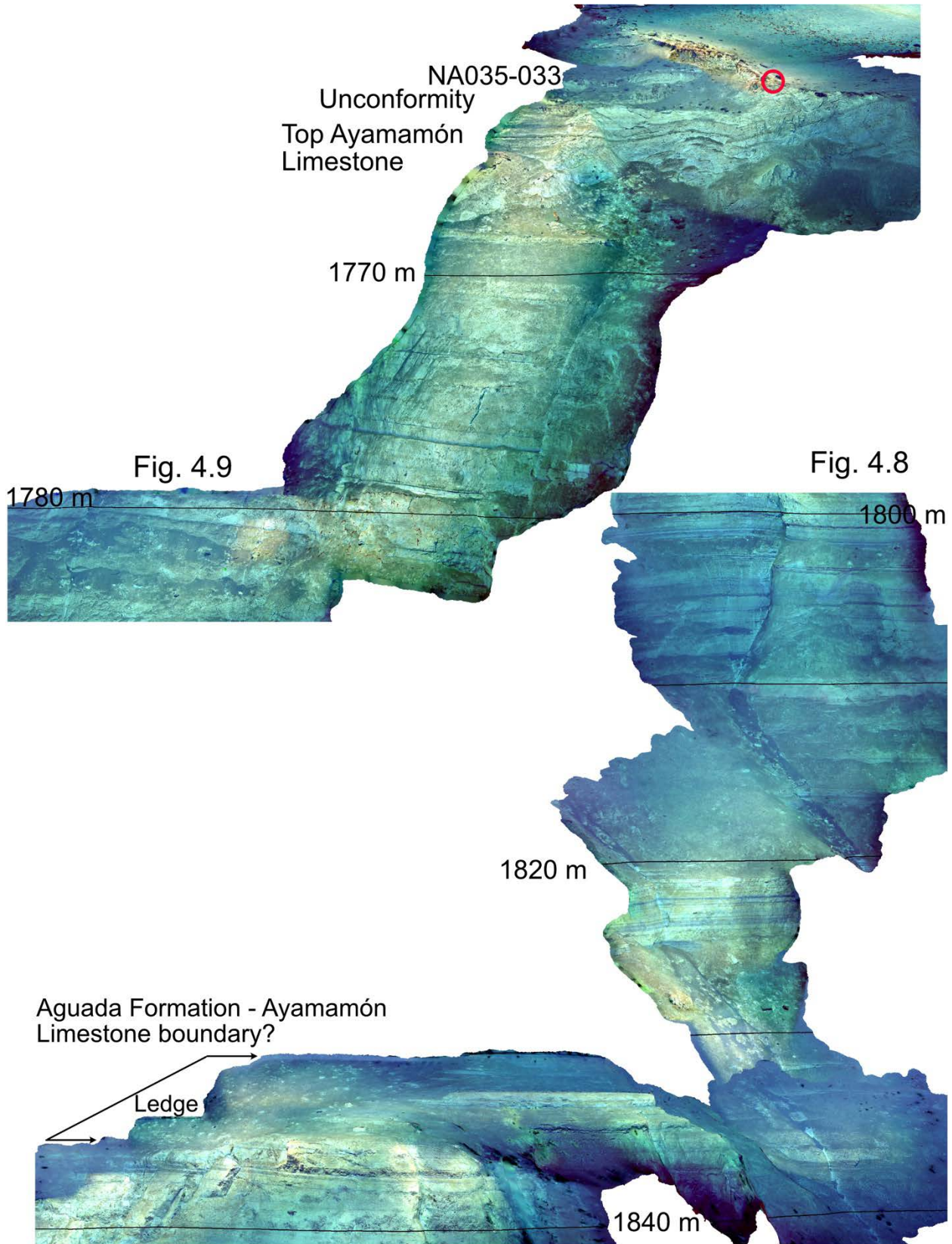


830

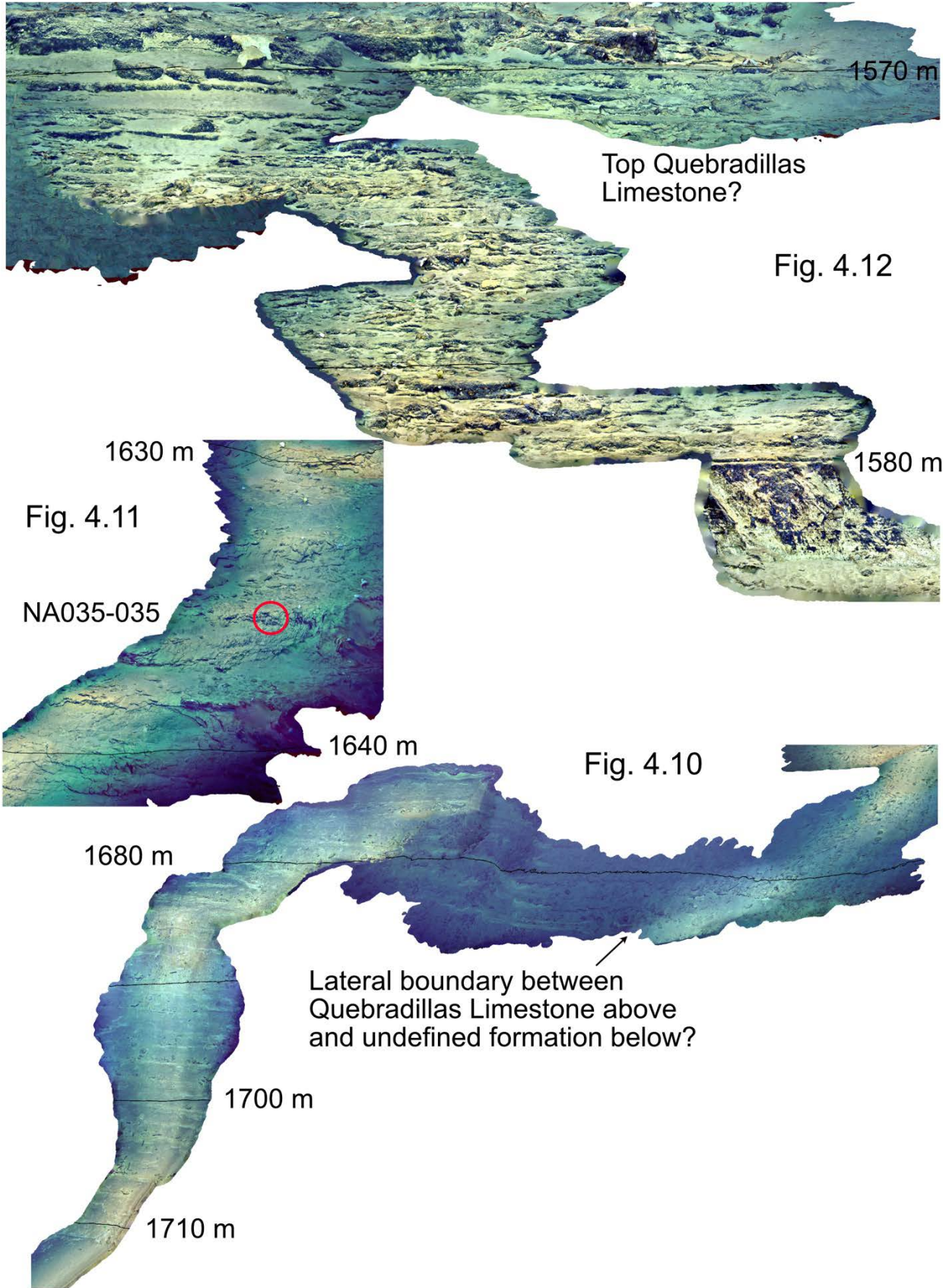
Fig. 4.7

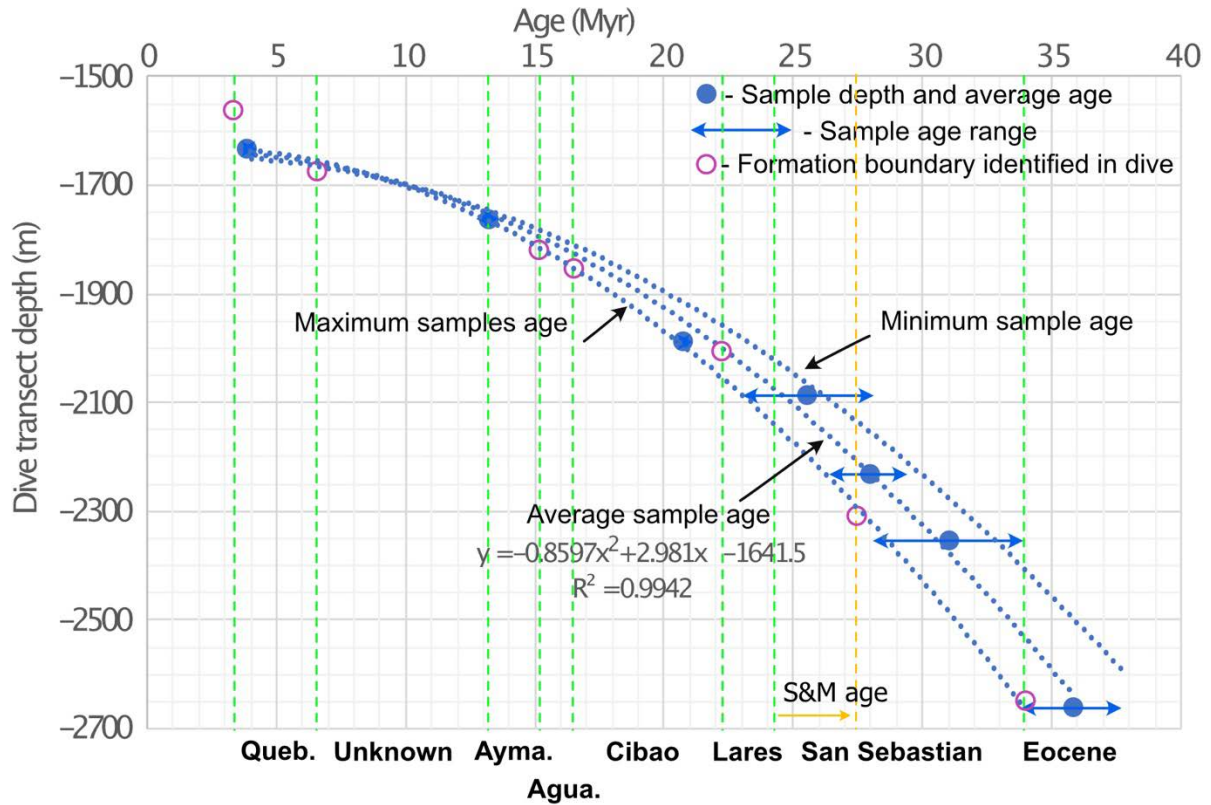


831



832

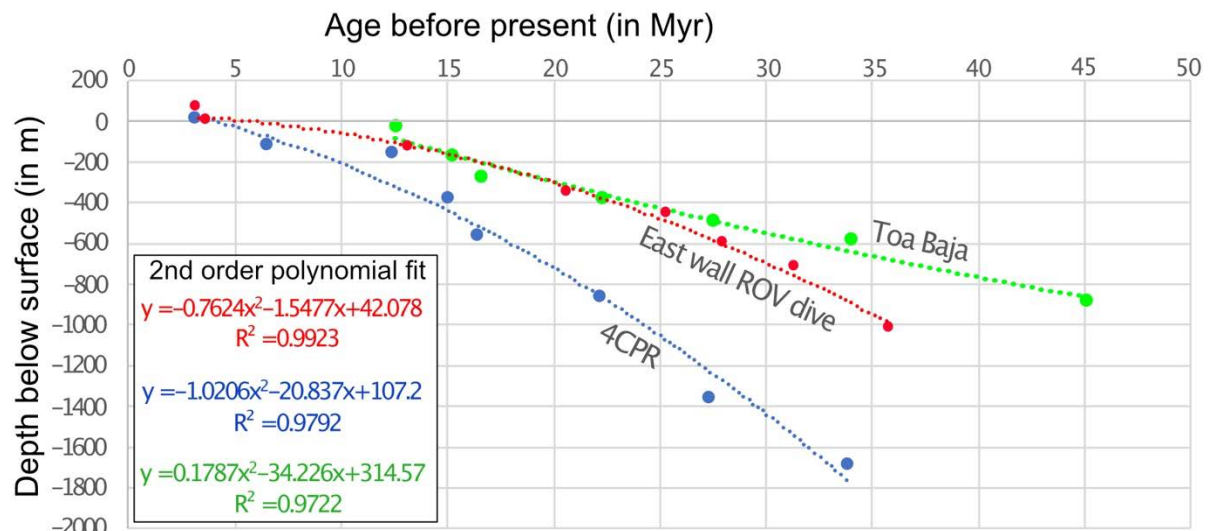




834

835 **Figure 5.**

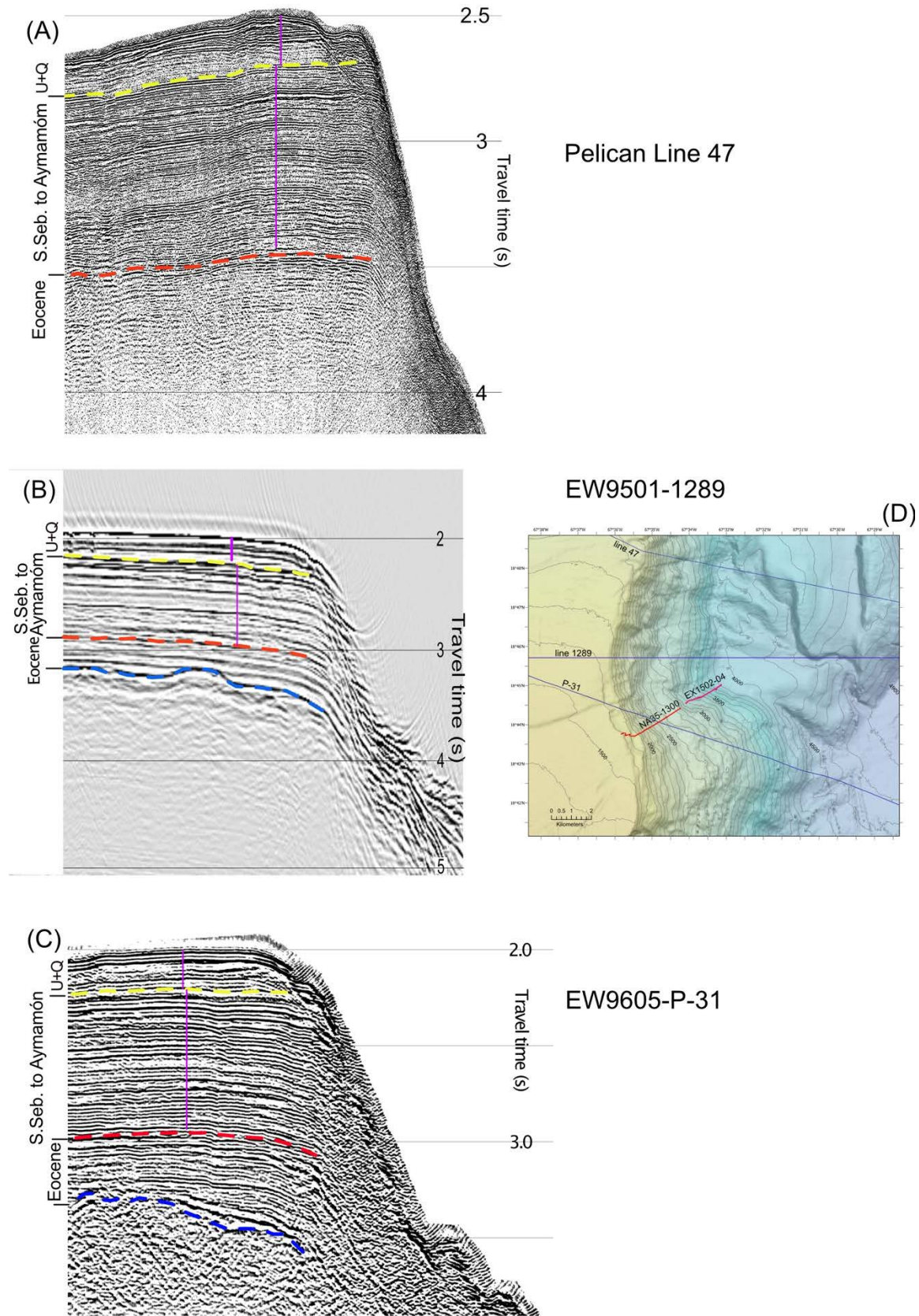
836



837

838 **Figure 6.**

839



840

841 *Figure 7*

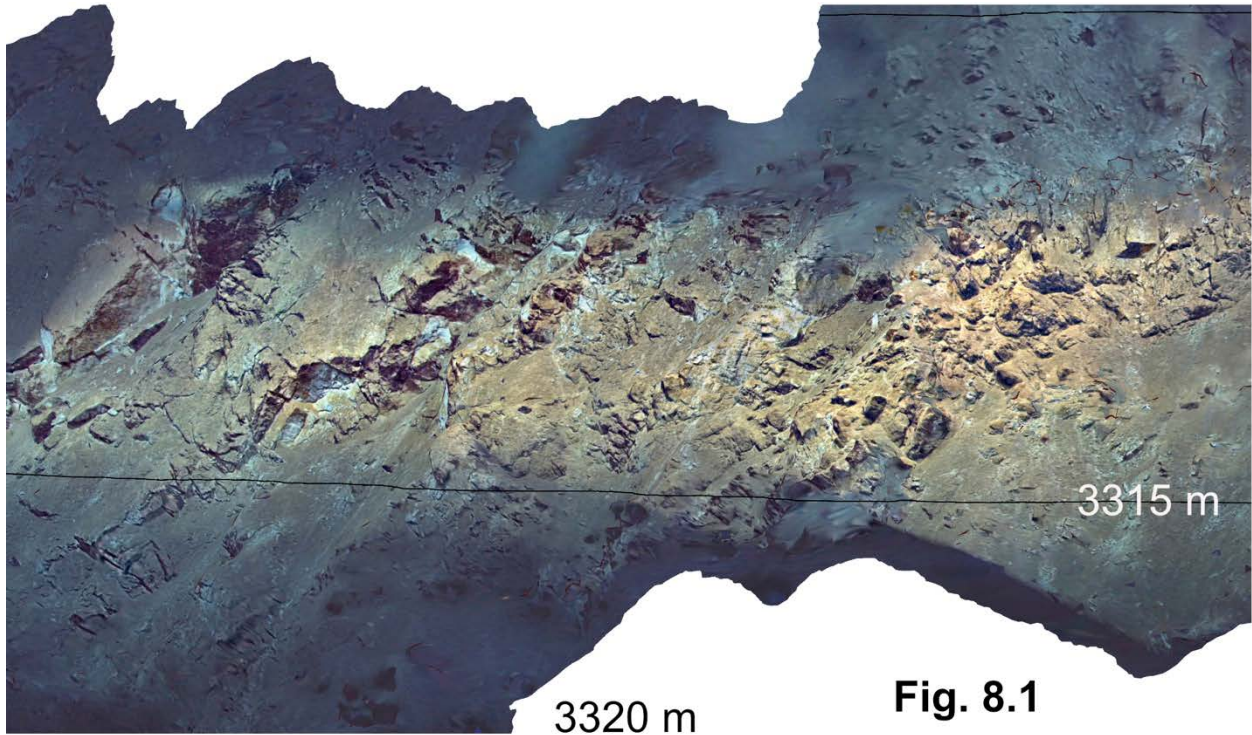


Fig. 8.1

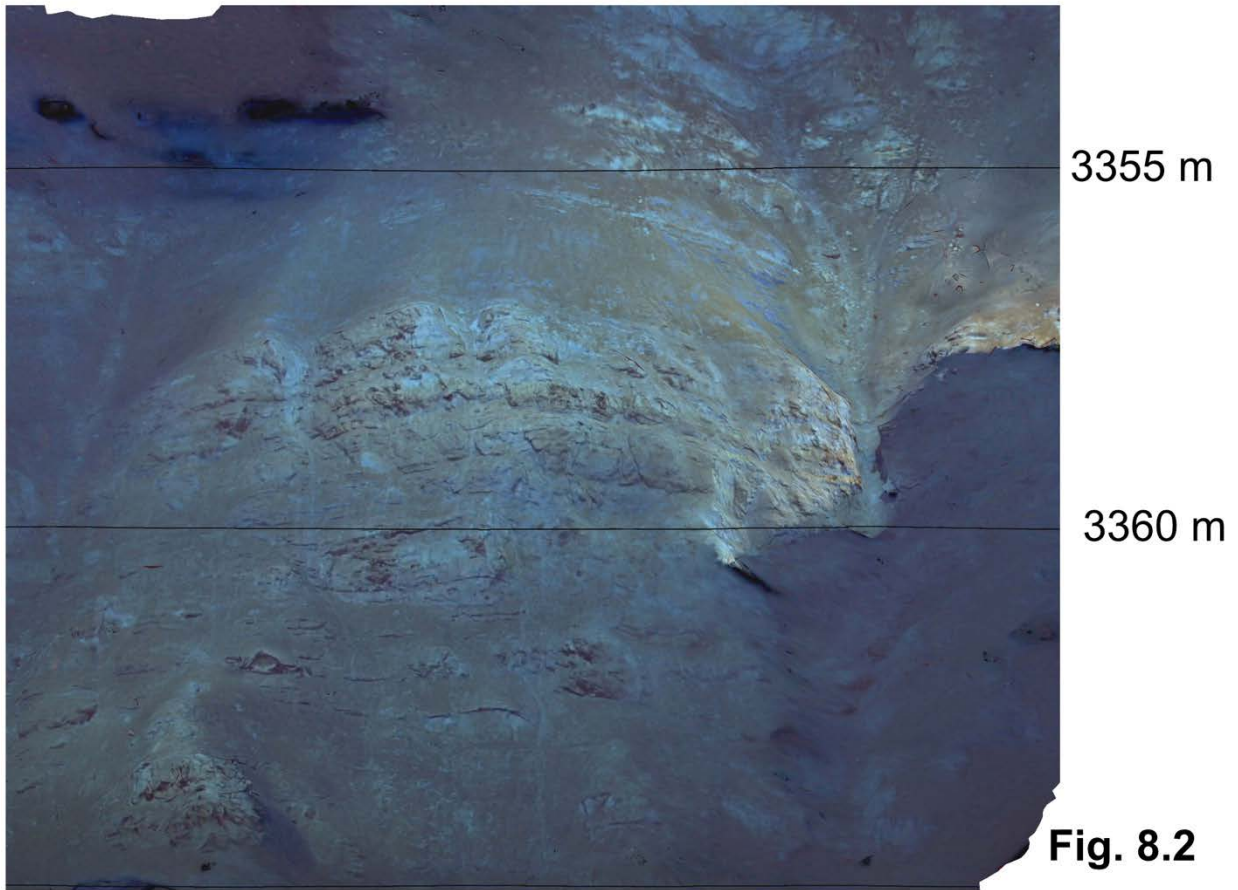


Fig. 8.2

842

Fig. 8.3

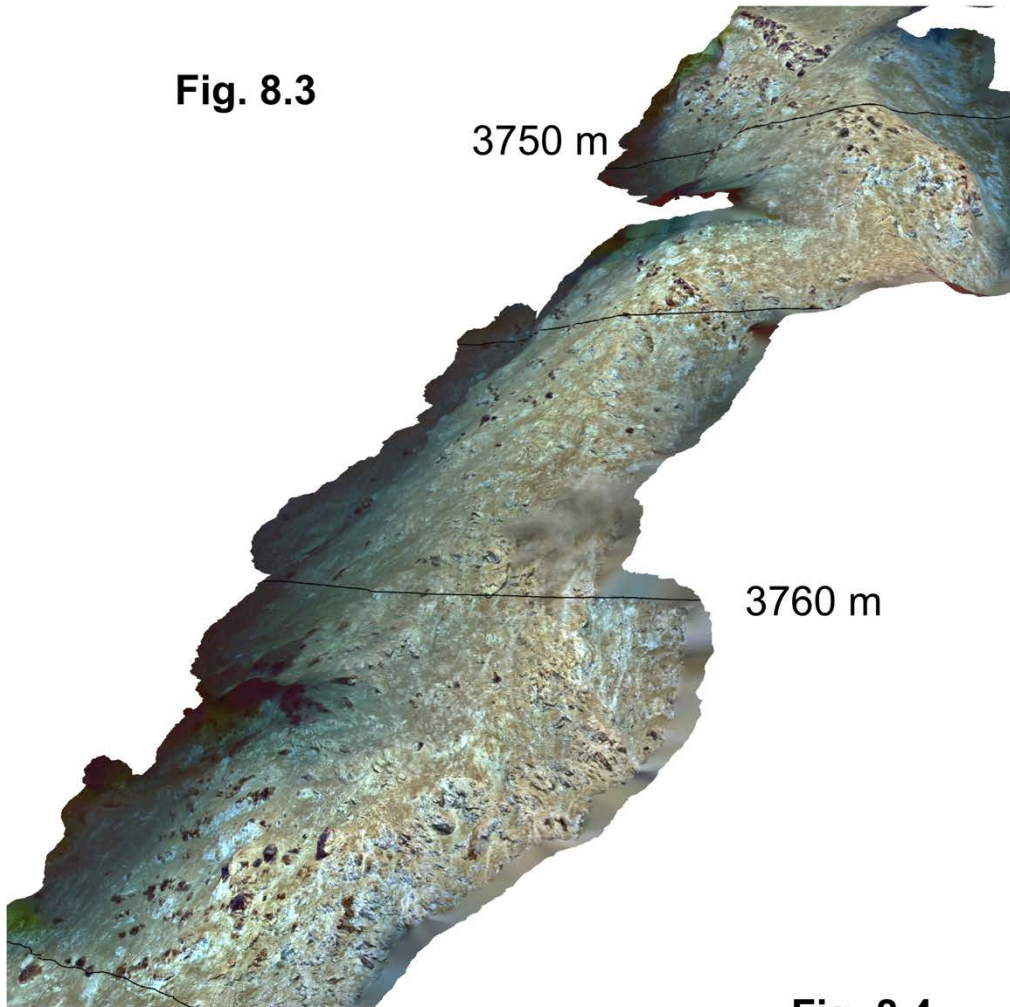
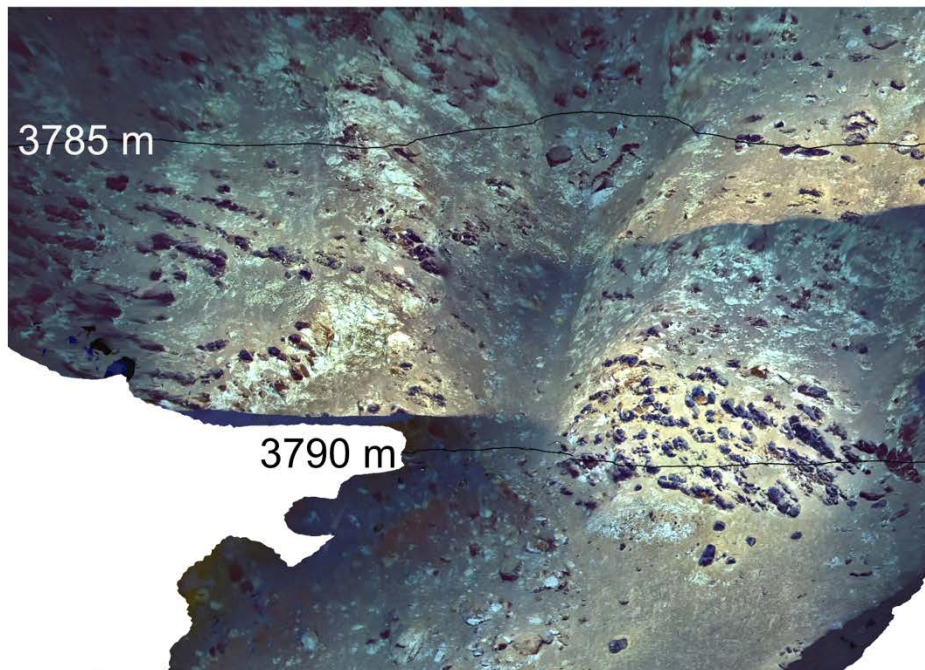
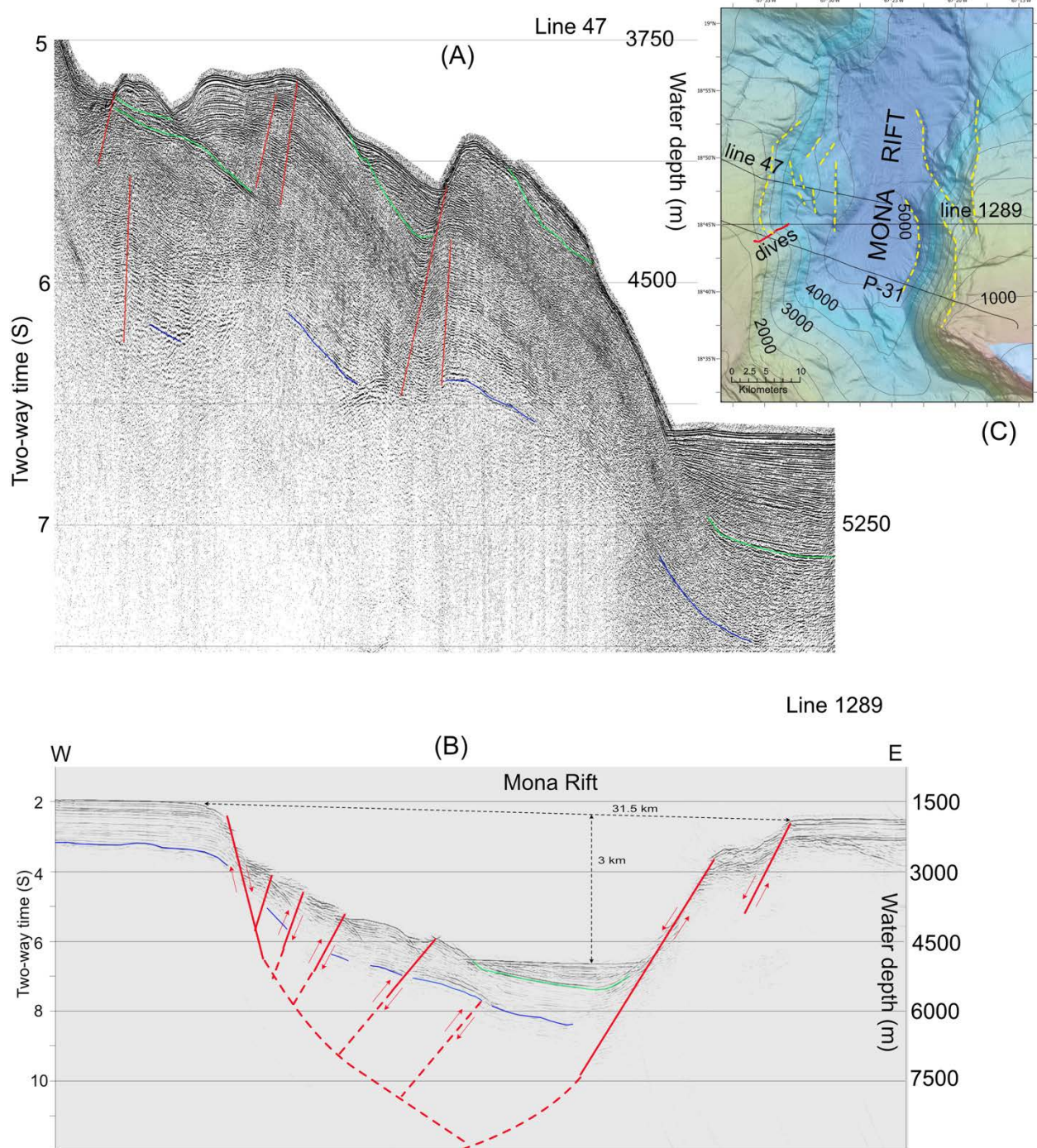


Fig. 8.4





844

845 **Figure 9**